Department of Physics and Astronomy

University of Heidelberg

Master thesis

in Physics

submitted by

Sofia Botsi

born in Chania

2017

Isotopic shift

measured with

a spin-orbit wave packet

This Master thesis has been carried out by Sofia Botsi

at the

Max-Planck-Institut für Kernphysik

under the supervision of

Priv.-Doz. Dr. Robert Moshammer

$\mu\varepsilon\theta'\ \ \eta\delta o\nu\eta\varsigma\ \ \mu\alpha\nu\theta\alpha\nu\varepsilon\iota\nu$

$A\rho\iota\sigma\tau o\tau\varepsilon\lambda\eta\varsigma$

Isotopenverschiebung gemessen mittels Spin-Orbit Wellenpaketdynamik

Die Messung von Isotopenverschiebungen in Edelgasen erlaubt hochpräzise Tests von relativistischen und quantenelektrodynamischen Effekten. In unserem Experiment wurde die Isotopenverschiebung zwischen ^{36}Ar und ^{40}Ar anhand des $3s^2 3p^5$ ($^2P_{3/2} \rightarrow {}^2P_{1/2}$) Übergangs in einfach ionisierten Argonatomen gemessen. Zu diesem Zweck wurde ein Ramsey-Experiment mit zwei ultrakurzen Laserpulsen ($\sim$ 6fs) implementiert. Der erste Puls (Pump-) präpariert die Atome in einer kohärenten Überlagerung der oben genannten Zustände. Die Dynamik des so entstandenen Spin-Orbit Wellenpakets kann mit einem zweiten, zeitverzögerten Puls (Probe-) untersucht werden. Um eine höhere Messpräzision zu erreichen, wurde ein Mach-Zehnder Interferometer so modifiziert, dass lange Zeitverzögerungen zwischen den Pulsen $(3.97ns)$ eingestellt werden konnten. Die Ionen der verschiedenen Argonisotope wurden in einem Reaktionsmikroskop (REMI) detektiert. Damit wurde die oben genannte Isotopenverschiebung auf einen Wert von $(1.22 \pm 0.10) \cdot 10^{-7}$eV bestimmt. Soweit wir wissen stellt dieses Experiment die erste Messung der Isotopenverschiebung dieses atomaren Übergangs dar.

Isotopic shift measured with a spin-orbit wave packet

High precision measurements of isotopic shifts in noble gases can provide a very good test of relativistic and quantum electrodynamic effects. In our experiment, we measured the isotopic shift between ^{36}Ar and ^{40}Ar for the $3s^2 3p^5$ ($^2P_{3/2} \rightarrow {}^2P_{1/2}$) transition for singly ionized argon atoms. We measured the shift by implementing a Ramsey scheme using two ultra-short ($\sim$ 6fs) laser pulses. The first laser pulse excites the system in a coherent superposition of the aforementioned states. This superposition leads to a spin-orbit wave packet whose dynamics can be investigated by applying a second delayed probe pulse. In order to increase the precision of a measurement, we modified a Mach-Zehnder interferometer, to introduce a long time delay of 3.97ns between the two pulses. To detect the ions of different argon isotopes we used a reaction microscope spectrometer (REMI). The isotopic shift is found to be $(1.22 \pm 0.10) \cdot 10^{-7}$eV and it is the first time it has been measured for this transition to the best of our knowledge.

Contents

1 Introduction **1**

2 Isotopic shifts in atomic spectra **5**
2.1 What is an isotopic shift? 5
2.2 Theoretical and experimental overview 6
2.3 The mass shift in optical spectra 10
2.3.1 The normal mass shift 11
2.3.2 The specific mass shift 12
2.4 The field shift in atomic spectra 12
2.5 Isotopic shifts in argon 14

3 Ultra short laser pulses and strong laser fields **17**
3.1 Ultrashort laser pulses 17
3.1.1 A short mathematical description 17
3.1.2 Kerr lens mode locking (KLM) 20
3.1.3 Dispersion compensation 21
3.2 Ionization in strong laser fields 22
3.2.1 Multiphoton and tunnel ionization 22
3.2.2 The ADK theory 24
3.3 The spin-orbit wave packet (SOWP) 25

4 Spectroscopic technique and experimental setup **29**
4.1 Spectroscopic technique 29
4.1.1 Rabi oscillations 29
4.1.2 Ramsey spectroscopy 31
4.1.3 Creating a spin-orbit wave packet 35
4.2 Experimental setup 36
4.2.1 The femtosecond laser system 36
4.2.2 Setup for the generation of few-cycle pulses . . 39
4.2.3 The Mach-Zehnder interferometer 41
4.2.4 The Reaction Microscope (ReMi) 43
4.2.4.1 Setup and some technical specifications 43

5 Measurement of the isotopic shift of ^{40}Ar and ^{36}Ar **49**
5.1 Data acquisition 49
5.2 Data calibration 52
5.2.1 Calibration using ^{40}Ar 52
5.2.2 Calibration using ^{36}Ar 59
5.3 Phase extraction 60
5.3.1 Measuring the isotopic shift 60
5.4 Interpreting the results 64

6 Summary and outlook **65**

A **67**
A.1 Atomic units (a.u.) and physical constants 67
A.2 Particle data 68

Bibliography **69**

Acknowledgements **77**

Chapter 1

Introduction

Scientists have always been interested in exploring the extremes starting from cosmological scales and going down to molecular, atomic and eventually electronic scales. In order to explore such processes, the limits of measurable length and time scales have to be exceeded by working beyond the natural frame of meter (m) and second (s). In practice, on the cosmological scale this corresponds to $10^{26}m$ and $10^{17}s$ and on the electronic scale to 1 Ångström (1Å=$10^{-10}m$) and one femtosecond ($1fs = 10^{-15}s$) or even 1 attosecond ($1as = 10^{-18}s$). The latter scale, which is studied in the context of ultrafast dynamics, has been in the center of fundamental research over the last decades in the field of atomic and molecular optical physics. This occurs mainly since it contributes to our better understanding of fundamental processes taking place in quantum mechanics.

However, the progress in the observation of processes faster than one second was done gradually. Initially, mechanical clocks were utlized which were eventually replaced by photographic devices. With the use of the latter, the microsecond range was reached ($1\mu s = 10^{-6}s$). The use of electronic devices based on semiconductor materials allowed the observation of the nanosecond regime ($1ns = 10^{-9}s$). But the breakthrough occured when T. H. Mainman invented the laser in 1960 [Mai60] which later led to the creation of ultrashort laser pulses. Nowadays, these pulses can have a duration of a few femtoseconds allowing in this way the observation of processes taking place on such short timescales. By solely using these pulses one can illuminate an ultrashort process but one cannot record them. This can be achieved by performing pump-probe experiments where two ultrashort laser pulses are required.

In these experiments the first pulse, the pump pulse, can interact with the system being investigated and initiate the dynamical process. The second pulse is quite stronger than the pump and it probes the dynamics of the system. Quite often a time-delay is introduced between the two pulses. This time-delay together with the duration of the pulses can affect the final resolution.

Over the last years the duration of optical laser pulses has been significantly decreased reaching the value of $2fs$. As a result, extremely high peak powers are produced since large amounts of energy are concentrated in short timespans. The intensity of such pulses

can reach values on the order of $10^{15} W/cm^2$ at which the strength of the electric field can be compared to the binding energy of the electrons to the nucleus. As a result, the pulse can modify the atomic or molecular target and more specifically the electric field of the laser can bend the Coulomb potential of the atom. The electron can tunnel into the continuum as described by L. Keldysh in 1965 who treated the laser field classically [KEL65]. A quantum description of the behavior of the electron after the tunneling, was provided by P.B. Corkum in 1993 in the *three step model* [Cor93].

In this thesis, we used laser pulses in pump-probe experiments in order to study the isotopic shift of the energy levels of ^{40}Ar and ^{36}Ar. Isotopic shifts have been a topic of continuous study over the last decades on both theoretical and experimental level since their better understanding can be useful for atomic and nuclear physics. The shift is reflected on the electronic binding energies of the atom and is a result of the finite mass and volume of the nucleus. Simultaneously, the fast developement of computers and the increase in computational power has helped theoreticians to investigate the properties of many-electron atoms. Additionally, laser spectroscopy has enabled experimentalists to observe isotopic shifts that could not be measured in the past. They concern transitions in rare isotopes or occuring at high-lying atomic levels. The accuracy of measurements is increasing continuously for both optical and x-ray transitions of muonic atoms. Finally, for a complete study on the isotopic shifts the relativistic effects in the atomic structure have to be taken into account.

In this experiment, the detection of ^{40}Ar and ^{36}Ar took place at a Reaction Microscope spectrometer. It is a highly advanced momentum spectrometer which can perform measurements of electrons and ions in coincidence. In our experiment we were only interested in the detection of ions. The time-of-flight, i.e. the time the ions need to reach the detector at the one edge of the Reaction Microscope and the hit x and y positions of the ions on the detector were recorded. The obtained data were calibrated and analyzed and the value of the total isotopic shift between ^{40}Ar and ^{36}Ar for the $3s^2 3p^5$ $(^2P_{3/2} \rightarrow {}^2P_{1/2})$ transition was measured. To the best of our knowledge, this is the first time that the isotopic shift of this transition is measured. This was a strong motivation for us to try and evaluate this shift. Additionally, the implementation of a novel experimental set-up and the use of a Ramsey-like spectroscopic technique has significantly increased the precision of our final value. Our aim is to apply this scheme to other noble gases in order to make this method universal. However, many questions still remain, including the exact calculation of the different contributions to the total isotopic shift.

This thesis is structured as follows: In Chapter 2 we introduce information necessary for the better understanding of the isotopic

shifts. A brief overview including some of the most significant theoretical and experimental achievements contributing to the study of the isotopic shifts is given. The different effects that contribute to the total isotopic shift are presented. The last section describes the present knowledge about isotopic shifts in argon.

Chapter 3 consists of three parts. In the first part, ultrashort laser pulses are described. Their creation and a short mathematical description is provided. Next, the *Kerr lens mode locking* method is reviewed and lastly the phenomenon of dispersion is discussed and some optical elements which compensate for it are presented. In the second part, some of the phenomena which occur in strong field physics are introduced. The two most significant pictures, i.e. the multiphoton and tunnel ionization are presented. Also, the ADK model is shortly introduced. In the last part, the creation of a *spin-orbit wave packet* is presented and a brief mathematical description is provided.

Chapter 4 gives information on the spectroscopic technique as well as the experimental apparatus used for this thesis. In the first part, the Rabi oscillations are presented as an introduction to Ramsey spectroscopy which is the spectroscopic technique used in this experiment. The way the spin-orbit wave packet was created in our scheme is presented. In the second part, the experimental set-up is described. This includes the femtosecond laser system, followed by a set-up for the generation of few cycle pulses. The Mach-Zehnder interferometer that was built and modified is presented as well. The working principle of the reaction microscope spectrometer and a few details concerning some of its technical characteristics are given.

In Chapter 5 the experimental results are presented in detail. The calibration procedure for both ^{40}Ar and ^{36}Ar is explained. Some of the most important parts of the data analysis are discussed. The analytical calculations for the determination of the isotopic shift are presented followed by a discussion and an interpretation of the results.

Finally, Chapter 6 includes a summary of the experiment performed and its results. It also gives an outlook on possible future studies based on the advancements developed and presented in the frame of this thesis.

Chapter 2

Isotopic shifts in atomic spectra

2.1 What is an isotopic shift?

We consider an atom consisting of a nucleus with atomic mass number $A = Z + N$, where Z is the number of protons and N is the neutron number. The atom is in the ground state and the electrons orbiting around the nucleus occupy states characterized by the quantum number n. In the atomic spectrum, the transition energies ΔE of the lines mostly depend on the number of protons, the number of electrons and the principal quantum number n. But if the system is studied more closely, a small dependance on the neutron number N is evident. This dependance is the so-called isotopic shift *(IS)* (or isotope shift). It is the small difference in the frequency of the spectral lines emitted by different isotopes of an element. This energy difference can occur in both atomic and molecular spectra but we will solely be interested in the former.

There are two mechanisms which give rise to differences in the energies of lines emitted by isotopes. The first is the *mass shift (MS)*, which is due to the different mass values of the isotopes and the second is the *field shift (FS)*, which arises from the different nuclear charge distributions in different isotopes.

For the mass shift, one has to consider that the value of the angular momentum of an energy level is fixed and that the total angular momentum has to be preserved. Therefore, if the atomic mass of the nucleus is changed the energy of the level is shifted. There are two contributions to the mass effect, namely the *normal mass shift (NMS)* and the *specific mass shift (SMS)*, which will be presented in more details below.

For the field shift (or also known as the volume effect), although different isotopes have the same number of protons, they are not distributed in the same way in space. The charge distribution creates an electric field which determines the energy of the electrons.

The total isotopic shift can be described to a good approximation by the equation:

$$IS = MS + FS = NMS + SMS + FS \tag{2.1}$$

In general, the mass shift dominates for lighter atoms whilst the field shift is more evident in heavier atoms [BDF03].

An isotopic shift has the same order of magnitude as the magnetic hyperfine splitting, i.e. they are relatively small in optical transitions (a few μeV). They are also present in x-ray transitions but the interactions of the inner electrons with the nucleus are stronger and therefore the shifts are larger (usually given in eV). In muonic x-rays, where a muon replaces the orbiting around the nucleus electron, the interaction between them is even stronger resulting in shifts of the order of a few keV. For instance, a typical large optical IS can have the following values in different units:

$$100mK = 0.1cm^{-1} = 19m^{-1} \equiv 3000MHz \equiv 12.3\mu eV \tag{2.2}$$

For the complete study of the isotopic shifts it is necessary to clarify when a shift is positive or negative. The convention that has been used through most of the literature is to describe an *IS* as positive when the frequency of the line of the heavier isotope is greater and negative otherwise. However, in most recent publications only relative level shifts are presented where the ground level is arbitrarily chosen to be zero.

2.2 Theoretical and experimental overview

The concept of isotopes was initially proposed by F. Soddy in 1913, for which he received the Nobel Prize in Chemistry in 1922 [Sod13]. The word is derived from the Greek *isos* (equal) and *topos* (place), the place being the place in the perodic table. Aronberg was the first one to successfully measure an isotope shift in 1918 [Aro18]. He investigated lead at a wavelength of 4058Å and noticed that the wavelength of ordinary lead was by 4.3mÅ smaller than the one of radio-lead. During that time the atomic weight of lead was determined by T.W. Richards to be 206.318 [RL14].

One of the first theoretical studies on isotopic shifts was the calculation of the *MS* in multi-electron atoms peformed by Hughes and Eckart in 1930. They first proposed that the *MS* can be separated into two components, namely the *NMS* and the *SMS*. They studied the effect of the motion of the nucleus observed in the spectrum of lithium and their results were in good agreement with the experiments held at that time [HE30]. Some first works on the *FS* came by Rosenthal and Breit in 1932 who tried to explain the deviations of the nuclear field from the inverse square law in PbI and PbII by using a relativistic theory [RB32]. At the same time Racah used the eigenfunctions of the relativistic equation with a Thomas-Fermi potential to calculate the relative displacement between two isotopes. The result for mercury was approximately $100cm^{-1}$ which was several times larger

than the experimental value of that time [Rac32]. Another notable contribution came from Crawford and Schawlow who corrected the approximation of the pertubation method and took into account the screening of inner electrons by the valence electron [CS49]. They also confirmed that the isotopic shifts of the ns electronic levels are proportional to $\psi^2(0)$. An overview of the results of the first half of the 20th century was published by Foster in 1951 [Fos51] and a couple of years later by Breit on the theoretical developments and calculations of the isotopic shifts [Bre58].

For the next two decades, research focused mostly on the study of the nuclear charge distribution between isotopes and more specifically theorists tried to understand which property of the nuclear charge was the one that was measured. The work of Bodmer [Bod58], Fradkin [Fra62] and Babushkin [Bab63] indicated that the *FS* term was the product of an electronic and a nuclear factor, where the latter was proportional to $\delta<r^2>$, the mean square radius of the nuclear charge. The estimation of the electronic factor was relatively easy but the nuclear factor was more difficult to calculate due to the uncertainty in knowledge of the electron screening. More insight into this effect was given by Wilson in 1968 who implemented Hartree-Fock calculations to study the screening effects on $|\psi(0)|^2$ for heavy atoms [Wil68].

Studies on isotopic shifts in muonic atoms were the subject of investigation during the following decade. Since the muon orbits closer to the nucleus than the electron, the *FS* is more pronounced. Fricke studied the interaction between the nucleus and the muon for the inner orbitals of muonic atoms and took into account the relativistic effects that influence the nuclear motion [Fri73]. Most of the developments up to that day on the theory of atomic isotopic shifts have been summarized in a review published by Bauche and Champeau [BC76]. Another interesting paper came from Palmer and Stacey [PS82] who explained the anomalous isotopic shifts observed in samarium by Griffith et al. [Gri+79]. The unsusual effects appearing in lines which connect two closely-spaced levels were theoretically treated by diagonalising the Hamiltonian describing those two levels.

Recently a lot of effort has been focused on the relativistic calculations of mass and field shifts mostly in heavier elements. Palmer proposed a reformulation of the evaluation of the *NMS* which includes relativistic corrections up to $1/c^2$ [Pal87]. Tupitsyn et al. indicated the significance of achieving high-precision measurements in highly charged ions as a test of relativistic and quantum electrodynamics in few electron systems. They used the relativistic recoil operator to evaluate the *MS* in Be- and B–like argon ions and found a good agreement between their theoretical calculations and experimental results [Tup+03]. Recently, new insight was brought into the subject from

Filippin et al., who proposed two computational approaches to estimate the mass- and field-shift factors in Al I [Fil+16]. The increase of computational power has significantly improved the accuracy of isotopic shift calculations especially over the last years. Simultaneously, the developments in experimental techniques have many times acted as a catalyst for the theoretical progress.

The experimental study of isotopic shifts required, even in its preliminary stage, a bright source for the acquisition of very sharp and narrow spectral lines. For this, in the first experiments performed, a Schüler tube was used in combination with a Fabry-Pérot etalon as an interferometer. The latter produced fringes which were photographed in high resolution and from them the spectrum of the studied isotope could be observed. Another possibility to obtain reasonably narrow and strong lines is to use an atomic beam as Jackson and Kuhn did in 1938. They utilized an electrodeless discharge tube filled with helium to observe the potassium resonance spectrum. They resolved the lines of ^{39}K and ^{41}K and measured a shift of $0.0076cm^{-1}$ whilst the theoretical prediction for hydrogen-like potassium was $0.0087cm^{-1}$ [JK38]. All the experimental results until that time have been collected and reviewed by Brix and Kopfermann [BK52].

More shifts were investigated with the increase in the availability of highly enriched isotopes. Also, precision was improved with the implementation in the experimental setups of photomultipliers, which are extremely sensitive detectors of light. Silver and Stacey used these developments in their study of the tin spectrum. Their spectroscopic data showed new values for the changes in the mean square radius which were significantly smaller than the already estimated numbers [SS73].

The measuring accuracy was improved significantly with the use of laser-spectroscopic techniques. The spectral line frequencies could be determined which was of fundamental importance for a better study of atomic processes. The spectrum of Xe was initially investigated with the use of a laser and an increase in accuracy from $3MHz$ to $300kHz$ was observed [BV66]. Although this improvement in precision enlighted new effects (like the fine structure of isotopic shifts), this technique could only be applied in a few transitions before the utilization of the tunable dye laser. Broadhurst et al. did use a continuous wave tunable dye laser to study the scattering from a well collimated atomic beam [Bro+74]. A photomultiplier measured the intensity of the scattered light as a function of the dye laser frequency. The cw laser was pumped by an argon ion laser whose bandwidth was limited to $17MHz$ FWHM. Additionally, the technique of Fourier transform spectroscopy has been used which enabled the measurement of shifts in many lines of a spectrum as was done in the case of mercury [GV75].

In the experimental study of the *FS*, a significant conclusion, concerning the nuclear charge distribution, was that as the neutron number increases, the charge distribution of the nucleons gets larger. Also, the charge distribution of nucleons with even atomic number is larger than their neighboring ones which have an odd atomic number. This result was provided by Shera et al. who studied the muonic x-ray spectra of five barium isotopes [She+82]. They studied the products of pion decays and the momenta of the muons produced were collected by a spectrometer. Another interesting point of this paper was the so-called "odd-even staggering effect", which arises when shifts between atoms with odd and even atomic number are studied. Isotopic shifts of Ba were further investigated at the $5d \rightarrow 6p$ transition, using fast ion beam-spectroscopy [Vil+93]. The case of barium indicates the significance of measuring isotopic shifts which can enhance our insight on the nuclear structure of different atoms, such as the mean square radii of the nuclear charge distribution.

More recently, the need to accurately test relativistic and quantum electrodynamic effects both theoretically as well as experimentally is even more profound. Therefore, relativistic calculations of isotope shifts can be used as a tool to achieve this high precision required. This subject was experimentally investigated by Soria Orts et al. in 2006 at the Heidelberg electron beam ion trap [Ort+06]. Among their results was the detection of the isotopic shift between ^{36}Ar and ^{40}Ar with sub-ppm accuracy. The theoretical value of this shift was also presented which agreed quite well with the experimental data. Another technique worth mentioning is that used by Gebert et al. which utilized quantum logic detection schemes to measure the isotopic shift in calcium ions [Geb+15]. They studied the $^2S_{1/2} \rightarrow {}^2P_{1/2}$ transition for $^{42}Ca^+$,$^{44}Ca^+$, and $^{48}Ca^+$ ions relative to $^{40}Ca^+$ with an accuracy below $100kHz$ indicating the precision of photon recoil spectroscopy. With this method, the absorption of photons can be detected via the investigated ion when the photon recoil is transfered on a co-trapped ion of different species [Wan+14].

A more detailed historical overview of the most significant achievements in the field of theoretical and experimental isotopic shifts can be found in [Kin13]. Further investigation on this topic is of great importance since it can significantly improve our knowledge on nuclear phenomena and can be very helpful to theorists who require a precise way to test the validity of relativistic and quantum electrodynamics. There are special cases (as deuterium for instance) for which shift measurements are the only possibility to study the size of small contributions of the electromagnetic interaction [BB76]. Simultaneously, the fast improvement of laser spectroscopic techniques has significantly contributed to atomic measurements, as the resolution of the studied lines can be increased for instance. Therefore, the study of isotopic shifts and isotopic separation as a laser application, is nowadays one of the most active research areas.

2.3 The mass shift in optical spectra

The mass effect in the case of one-electron atoms can be physically interpreted by the fact that the nucleus is not at the center of mass of the atom, but instead, together with electrons, it orbits around the centre of the system. For a mathematical description of this effect the following article was followed [Joh01] which is based on earlier calculations conducted by Mårtensson and Salomonson in 1982. We will consider a non-relativistic atom, consisting of a nucleus of mass M_A placed at $\overrightarrow{r_0}$ and N electrons of mass m_e at $(\overrightarrow{r_1}, \overrightarrow{r_2}, ...)$. The Hamiltonian which desribes the $N+1$ particle atom is:

$$\begin{aligned} H(\overrightarrow{r_0}, \overrightarrow{r_1}, \overrightarrow{r_2}, ..., \overrightarrow{p_0}, \overrightarrow{p_1}, \overrightarrow{p_2}, ...) = \frac{p_0^2}{2M_A} + \sum_i \frac{p_i^2}{2m_e} \\ + \sum_i V_{e-N}(\overrightarrow{r_i} - \overrightarrow{r_0}) + \frac{1}{2}\sum_{i \neq j} V_{e-e}(\overrightarrow{r_i} - \overrightarrow{r_j}) \end{aligned} \tag{2.3}$$

The first two terms represent the kinetic energy of the nucleus and of the N electrons, whilst the last two terms indicate the interaction between the electrons and the nucleus and the interactions between the electrons respectively. We will work in the reference frame in which the center-of-mass of the atom is at rest and in which the coordinates transform according to:

$$\overrightarrow{\rho_i} = \overrightarrow{r_i} - \overrightarrow{r_0}$$

$$\overrightarrow{R} = \frac{M_A \overrightarrow{r_0} + m_e \sum_i \overrightarrow{r_i}}{M_A + N m_e} \tag{2.4}$$

The generalized momenta conjugate to $\overrightarrow{\rho_i}$ and $\overrightarrow{R}$ are:

$$\overrightarrow{\pi_i} = \frac{1}{i}\overrightarrow{\nabla}_{\rho_i}$$

and

$$\overrightarrow{P} = \frac{1}{i}\overrightarrow{\nabla}_R \tag{2.5}$$

respectively. By substituting equations 2.4 into equations 2.5 and performing the calculations we obtain:

$$\overrightarrow{\rho_i} = \overrightarrow{\pi_i} + \frac{m_e}{M_A + N m_e}\overrightarrow{P} \tag{2.6}$$

$$\overrightarrow{\rho_0} = -\sum_i \overrightarrow{\pi_i} + \frac{M_A}{M_A + N m_e}\overrightarrow{P} \tag{2.7}$$

We replace equation 2.6 and 2.7 into equation 2.3 and the kinetic term becomes:

$$\begin{aligned} E_{kin} &= \frac{1}{2m_e}\Big[\sum_i \overrightarrow{\pi}_i^2 + 2\frac{m_e}{M_A+Nm_e}\sum_i \overrightarrow{\pi}_i \cdot \overrightarrow{P} + \frac{Nm_e^2}{(M_A+Nm_e)^2}P^2\Big] \\ &+ \frac{1}{2M_A}\Big[(\sum_i \overrightarrow{\pi}_i)^2 - 2\frac{M_A}{M_A+Nm_e}\sum_i \overrightarrow{\pi}_i \cdot \overrightarrow{P} + \frac{M_A^2}{(M_A+Nm_e)^2}P^2\Big] \\ &= \frac{m_e+M_A}{2m_eM_A}\sum_i \overrightarrow{\pi}_i^2 + \frac{1}{M_A}\sum_{i\neq j} \overrightarrow{\pi}_i \cdot \overrightarrow{\pi}_j + \frac{1}{2(M_A+Nm_e)}P^2 \end{aligned} \tag{2.8}$$

The kinetic part of the Hamiltonian is seperated into a part which describes the center of mass motion and a part which describes the motion of N electrons relative to the nucleus. We are interested in the relative motion given by the Hamiltonian:

$$\begin{aligned} H(\overrightarrow{\rho_1}, \overrightarrow{\rho_2}, ..., \overrightarrow{\pi_1}, \overrightarrow{\pi_2}, ...) = &\sum_i \frac{\overrightarrow{\pi}_i^2}{2\mu} + \frac{1}{M_A}\sum_{i\neq j} \overrightarrow{\pi}_i \cdot \overrightarrow{\pi}_j \\ &+ \sum_i V_{e-N}(\overrightarrow{\rho_i}) + \frac{1}{2}\sum_{i\neq j} V_{e-e}(\overrightarrow{\rho_i} - \overrightarrow{\rho_j}) \end{aligned} \tag{2.9}$$

where $\mu = M_A m_e/(M_A + m_e)$ is the reduced mass.

2.3.1 The normal mass shift

The normal mass shift contains only the squares of the momenta of single electrons (i.e. the first term of 2.9) and thus is directly proportional to the reduced mass of the system μ. Its two natural limits are the positronium, for which $\mu = \frac{1}{2}m_e$ and an infinitely heavy nucleus, for which $\mu = m_e$. The shift is profound in all levels of all atomic systems and it always has a positive value [BB76]. For its mathematical description we will separate 2.9 into two parts, namely:

$$H(\overrightarrow{\rho_1}, \overrightarrow{\rho_2}, ..., \overrightarrow{\pi_1}, \overrightarrow{\pi_2}, ...) = H_\mu + \Delta H \tag{2.10}$$

where

$$H_\mu(\overrightarrow{\rho_1}, \overrightarrow{\rho_2}, ..., \overrightarrow{\pi_1}, \overrightarrow{\pi_2}, ...) = \sum_i \frac{\overrightarrow{\pi}_i^2}{2\mu} + \sum_i V_{e-N}(\overrightarrow{\rho_i}) + \frac{1}{2}\sum_{i\neq j} V_{e-e}(\overrightarrow{\rho_i} - \overrightarrow{\rho_j}) \tag{2.11}$$

and

$$\Delta H(\overrightarrow{\pi}_1, \overrightarrow{\pi}_2, ...) = \frac{1}{M_A}\sum_{i\neq j} \overrightarrow{\pi}_i \cdot \overrightarrow{\pi}_j \tag{2.12}$$

The first term of equation 2.11 corresponds to the normal mass shift and leads to a shrinking of the whole spectrum by a factor of μ/m_e. In the case of two isotopes with masses M_H and M_L (the heavy and the light one respectively) the fractional shift in frequency becomes:

$$\frac{v_H - v_L}{v_H} = \frac{m_e(M_H - M_L)}{M_H(M_L + m_e)} \quad , \quad \frac{v_H - v_L}{v_L} = \frac{m_e(M_H - M_L)}{M_L(M_H + m_e)} \tag{2.13}$$

For instance, the normal mass shift between deuterium and protonic hydrogen is $v_{2H} - v_{1H}/v_{1H} = 2.721 \cdot 10^{-4}$. For heavier elements, such as Pb, it is significantly decreased and for the $^{208}Pb - ^{206}Pb$ pair it takes the value of $2.56 \cdot 10^{-8}$. The former description can also be utilized for the study of a muonic system.

2.3.2 The specific mass shift

The specific mass shift term is given from equation 2.12 which contains only cross products of the electrons momenta. This phenomenon arises when the atom consists of more than one electron as can be seen in section 6.2.1 of [Foo05]. Its calculation is a non-trivial many body problem. The value of the shift is:

$$\delta E_{SMS} = \frac{1}{M_A}\left\langle \sum_{i \neq j} \overrightarrow{\pi}_i \cdot \overrightarrow{\pi}_j \right\rangle \tag{2.14}$$

The correlations in the motion of the electrons can influence the value of the specific mass shift, which can be either negative or positive [HS74]. Its precise estimation, however, requires more complex calculations which will not be examined here.

Finally, the mass shift effect, including both of the aforementioned contributions, is treated in the relativistic theory in the framework of QED since it naturally originates from the relativistic nuclear recoil operator. A detailed theoretical explanation can be found in [Sha98].

2.4 The field shift in atomic spectra

The field shift arises from the change in the electric charge distribution of the nucleus due to the different number of neutrons between isotopes. Since the nucleus has a finite size, the electrostatic nuclear potential will differ from $1/r$ which is used when the nucleus is considered point-like. Still following the description of [Joh01], the energy difference between two isotopes can be approximated by:

$$\delta E = -F\delta\langle r^2 \rangle \tag{2.15}$$

where F is the field shift factor and $\delta\langle r^2 \rangle$ is the mean-square charge radius difference. For the evaluation of those two terms the nucleus

will be considered as a homogeneously charged sphere of radius R and thus the nuclear potential is:

$$V(r,R) = \begin{cases} -(Z/2R)[3 - r^2/R^2] & , \quad r < R \\ -Z/r & , \quad r \geq R \end{cases} \tag{2.16}$$

By inducing a change δR inside the radius, the potential becomes:

$$\delta V = \frac{3Z}{2R^2}\Big[1 - \frac{r^2}{R^2}\Big]\delta R, \quad r \leq R \tag{2.17}$$

For a uniform distribution the root mean square charge radius of the nucleus is:

$$\delta\langle r^2\rangle = \frac{1}{Ze}\int d^3r\rho(r)r^2 = \frac{3R^2}{5} \tag{2.18}$$

Therefore, equation 2.17 becomes:

$$\delta V = \frac{5Z}{4R^2}\Big[1 - \frac{r^2}{R^2}\Big]\delta\langle r^2\rangle, \quad r \leq R \tag{2.19}$$

The single particle operator is:

$$H_{nuc} = -\frac{5Z}{4R^2}\Big[1 - \frac{r^2}{R^2}\Big] \tag{2.20}$$

From this, the field-shift parameter can be derived, namely:

$$F = \langle H_{nuc}\rangle \tag{2.21}$$

The field shift is more evident for heavier elements since the nuclear charge increases with the proton number Z. Additionally, the nuclear property of polarization of the nucleus by the electrons can have an effect on atomic structure. In their study of spectroscopic isotopic shifts, Breit et al. investigated the order of magnitude of polarization effects of a nucleus by atomic electrons [BAC50]. They concluded that those effects can be quite significant and one of the main factors responsible for the shifts. Analytical calculations on the nuclear polarization energy shifts for one-electron ions can be found in [Nef+96].

The need for a deeper understanding of the nuclear structure and for accurately determining the nuclear radius mean square radii has increased the significance of isotopic shift measurements. Over the last decades, the experiments in atomic physics have become more precise and simultaneous improvement has been observed in the theoretical calculations of electronic energies. However, it is not trivial

to perform atomic physics experiments in order to obtain information about nuclear effects. Therefore, a straightforward experimental technique can be of great value for the fast and accurate determination of those shifts.

2.5 Isotopic shifts in argon

Argon was discovered by Lord Rayleigh and Sir William Ramsay in 1894 and the first isotopic shift measurement in its spectrum was performed by Kopfermann and Krüger in 1937 [KK37]. Argon has an atomic weight of 39.948(1) and five main stable isotopes. The most common ones are ^{40}Ar with a relative abundance of 0.996035, ^{38}Ar with an abundance of $0.000629(7)$ and ^{36}Ar with an abundance of $0.003336(21)$ [Nis]. In the context of this thesis the isotopic shift between ^{36}Ar and ^{40}Ar is measured. The purity of the argon sample used was very high, reaching 99.998% and containing the different isotopes with their natural abundance.

Figure 2.1 includes some measurements of the total IS between ^{40}Ar and ^{36}Ar. In the first column of the table, the transition studied is depicted. In the second column the wavelength corresponding to each transition is shown. The energy separation of the transitions studied can also be seen in the third column of the table. It is more convenient to compare the transition energy with the *IS* and observe how small the latter is compared to the former. The last column depicts the experimental values of the the total *IS* which are of the order of several MHz. In all values systematic errors are included. More information on the shifts can be obtained from muonic data and elastic electron scattering [FHS04].

The atomic mass of argon indicates that the biggest contribution to the isotopic shift should arise from the mass effect. In figure 2.1 only the total *IS* can be seen though. For the interested reader the following paper is suggested [DPS99], where the contributions of the *NMS*, the *SMS* and the *FS* have been calculated seperately for most of the transitions depicted in figure 2.1. According to D' Amico et al., the contribution from the *NMS* to the total *IS* is much larger than the contribution of the *SMS* for the transitions studied. The contribution from the *FS* is much smaller compared to the others but nevertheless not negligible.

More recent measurements on the isotopic shift in highly charged argon ions indicate the need of following a fully relativistic treatment of the nuclear recoil effect and formulating it within quantum electrodynamics. When doing so, the contributions of the relativistic *NMS* and the relativistic *SMS* arise, which increase the precision of the total isotopic shift calculation and therefore it is necessary to take them into account. It is clear that further improvement on the precision of the already existing values can and needs to be reached. That is because isotopic shift measurements can significantly improve our

Isotopic shift measurements for ^{40}Ar and ^{36}Ar			
Transition	$\lambda[nm]$	E [eV]	$\delta\upsilon_{36-40}[MHz]$
$4s[3/2]_2 \rightarrow 4p[5/2]_3$	811.75	1.52	450.1(0.9)
$4s[1/2]_0 \rightarrow 4p[3/2]$	772.64	1.60	492.4(0.9)
$4s[3/2]_0 \rightarrow 4p[3/2]$	772.59	1.60	494.2(1.0)
$4s[3/2]_2 \rightarrow 4p[5/2]_3$	763.72	1.62	494.9(0.8)
$4s[3/2]_1 \rightarrow 4p[1/2]_0$	667.91	1.86	666.1(2.4)
$4s[3/2]_2 \rightarrow 4p[5/2]_3$	604.49	2.05	492.4(0.9)
$4p[5/2]_2 \rightarrow 5d[7/2]_3$	604.49	2.05	818.8(0.4)
$4p[5/2]_3 \rightarrow 5d[7/2]_4$	603.38	2.05	861.9(8)

FIGURE 2.1: Measurements of the total isotopic shift between ^{40}Ar and ^{36}Ar in the optical regime. The various transitions studied are shown together with the wavelength corresponding to each one of them as well as with the energy separation of the two levels. All of the shifts investigated are of the order of several MHz. Figure adapted from [DPS99].

knowledge concerning the atomic structure and more specifically the nucleus. As occured in the past for the case of samarium, it is also possible that such invesigations can bring to light new nuclear phenomena.

Additionally, not all transitions have been investigated up until now both on an experimental and a theoretical level. This, in combination with the implementation of a straightforward experimental technique, has been a motivation for us for a deeper study of the isotopic shifts in argon. The electronic configuration studied is the $3s^2 3p^5$ for the term $^2P^0$ between the states with a total angular momentum of $J = 3/2$ and $J = 1/2$. The shift is measured by using Ramsey-like spectroscopy with two strong and ultrashort laser pulses. The first pulse creates a coherent superposition of the two aforementioned states where the spin-orbit wave packet has a beating period of $23fs$. The second pulse probes the system after a delay of approximately $3ns$. This pump-probe scheme is applied on an argon gas jet containing the different isotopes and those are differentiated through mass spectrometry in our spectrometer chamber, a Reaction Microscope.

In the first part of next chapter a brief description of the intense and ultrashort laser pulses and their properties will be provided. Moreover, the ionization processes taking place in strong laser fields will be presented. The last part of the next chapter includes a brief

mathematical description of the creation and evolution of a spin-orbit wave packet between the two atomic states studied.

Chapter 3

Ultra short laser pulses and strong laser fields

3.1 Ultrashort laser pulses

One way to accurately study an isotopic shift is by exciting the quantum states participating in the transition of interest. The energy difference of these states indicates the speed of motion. Since we are investigating the motion of the valence electrons of the $^2P^0$ shell we are expecting this motion to take place at a subfemtosecond or even a few femtosecond regime. Strong-field physics is concerned with phenomena which take place at these timescales and arise from the interaction of strong electric fields with matter, i.e. atoms, molecules or solids, etc. The magnitude of those electric fields can be compared to the strength of the electron binding field and therefore cannot be neglected. These field intensities range from $10^{13} to 10^{18} W/cm^2$. Such strong laser fields can be created by intense ultrashort laser pulses. A short mathematical description of those pulses and their interaction with optical media is the topic of the first part of this chapter. In the second part, two ionization processes occuring in the presence of strong laser fields will be briefly presented. The last part consists of a short description of the *spin-orbit wave packet*.

3.1.1 A short mathematical description

Ultrashort laser pulses can be described as coherent bursts of electromagnetic radiation, confined in space and time. Temporal and spatial coherence, energy and intensity are amongst some of the most useful parameters used for their description. The temporal and the spatial properties of the electric field of the pulse can be presented in two different pictures, namely the frequency domain-representation and the time-domain representation which are connected by the Fourier transform. The mathematical description proposed by [DR06] and [Rul+05] has been followed in which only the electric part of the electro-magnetic field has been described. An ultrashort laser pulse

can be written as the product of two quantities, a time varying envelope $A(t)$ and a periodic function with frequency ω_0:

$$E(t) = A(t)cos(\omega_0 t + \phi_\omega) = Re[A(t)e^{i(\omega_0+\phi_\omega)}] \tag{3.1}$$

where ϕ_ω is the phase offset between $A(t)$ and the carrier wave.

An analytical expression for the electric field which includes the complex term is:

$$E(t) = \frac{1}{2}(\tilde{E}(t) + \tilde{E}^*(t)) = \frac{1}{2}(A(t)e^{i(\omega_0 t+\phi_\omega)} + A(t)e^{-i(\omega_0 t+\phi_\omega)}) \tag{3.2}$$

However, only the real part of this equation will be used in the following analysis.

It is convenient to write the electric field in both time and frequency domain. We obtain the latter by Fourier transforming the electric field and thus one can ontain the spectral amplitude of the pulse:

$$E(\omega) = \mathcal{F}[E(t)] = \int_{-\infty}^{+\infty} E(t)e^{-i\omega t}\, dt \tag{3.3}$$

The inverse Fourier transform is given by:

$$E(t) = \mathcal{F}^{-1}[E(\omega)] = \frac{1}{2\pi}\int_{-\infty}^{+\infty} E(\omega)e^{i\omega t}\, d\omega \tag{3.4}$$

From equation 3.4 one can see that the total electric field $E(t)$ consists of a superposition of oscillating fields, each one contributing to the total field by an amplitude $\mathcal{A}(t)$ which has its own phase ϕ_ω. Also, the spectral width limits the duration of the laser pulse. The knowledge of phase and amplitude in the Fourier domains is enough in order to represent the pulse in the time domain.

The envelope function can be approximated by a Gaussian:

$$A(t) = A_0 \exp\Big(-4\ln 2\Big(\frac{t}{\tau_{FWHM}}\Big)^2\Big) \tag{3.5}$$

where A_0 is the maximum amplitude and τ_{FWHM} is the Full width at Half maximum (FWHM) of the electric field envelope. For such Gaussian pulses the relation between the time duration of the laser pulse τ and the spectral bandwidth $\Delta\omega$ is:

$$\Delta\omega \cdot \tau \geq 2\pi c_B \tag{3.6}$$

where $c_B = 0.441$. This is the *bandwidth theorem* and when the equality holds the pulses are called *Fourier-limited*.

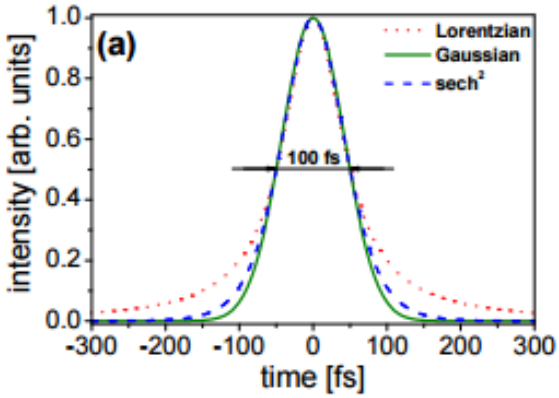

FIGURE 3.1: Ultrashort laser pulses of different shapes. A *Lorentzian* distribution is depicted with red dots, the green line represents a *Gaussian* distribution and the blue dotted plot is of the form $sech^2$. In all cases the full width at half maximum (FWHM) is 100fs. The picture is taken from [Shc09].

An ultrashort laser pulse can be seen in figure 3.1 for three different distributions. The intensity spectrum has been calculated for a Lorentzian, a Gaussian and a $sech^2$ distribution all with the same FWHM. A more detailed mathematical description of ultrashort laser pulses and the way they can be generated can alternatively be found in [KA93], [Fre95],[Boy03] and [Dem13].

For the generation of short laser pulses a broader bandwidth is necessary. The titanium-sapphire (Ti:Sa) laser is a good candidate concerning this, since an ultrabroad emission bandwidth pumped by a green laser is possible and simultaneously it has a high damage threshold. The spectroscopic and laser characteristics of the first Ti:Sa laser were discussed by Moulton in 1985 [Mou86]. The shortest pulses possible will be produced when all the modes created oscillate in phase. The frequency of two adjacent resonator modes is given by:

$$\Delta v = \frac{c}{2d} \tag{3.7}$$

where c is the speed of light and d is the cavity length.

Two equidistant modes oscillating with the frequency difference given in equation 3.7 in a phase locked manner result in the creation of single pulses propagating inside the laser cavity. This mode of operation is known as *mode locking* and it produces Fourier-limited pulses. There are two techniques for producing mode-locking in a laser, namely the *active* and the *passive* mode locking. The former can utilize an acousto/electro-optic modulator for instance, for the periodic modulation of the resonator losses. If this modulation gets synchronized with the resonator round trips, which have a period of T_R, the production of picosecond pulses is possible. To obtain

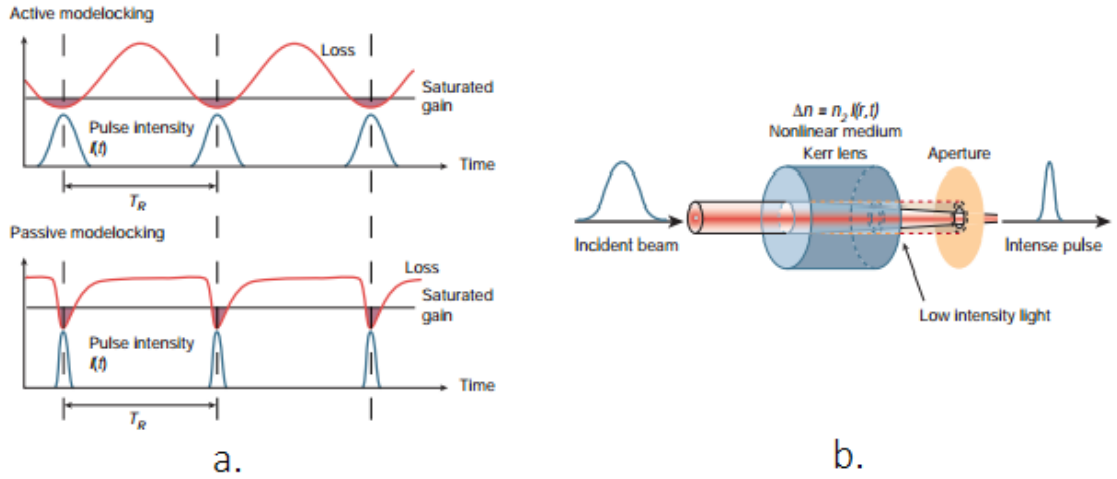

FIGURE 3.2: a) Active and passive mode-locking schematic set-up for the generation of ultrashort laser pulses. b) Kerr lens mode locking. It is a passive mode locking method which can produce ultrashort laser pulses on the order of a few femtoseconds [Kel03].

even shorter laser pulses, on the order of a few femtoseconds, passive mode-locking can be performed. For this technique pulses can be produced without a signal external to the laser. Alternatively, the light in the cavity is used in order to cause a change at some element inside the cavity. This change itself can modify the intracavity light.

Active and passive mode locking can be compared in the first picture of figure 3.2. Several techniques have been implemented in order to obtain mode locking operation, with the most popular one being the *Kerr lens mode locking* (KLM), briefly described in the following section.

3.1.2 Kerr lens mode locking (KLM)

Kerr lens mode locking (KLM) is a way to mode lock lasers by using a nonlinear optical process, namely the optical Kerr effect. The optical Kerr effect arises when an electric field changes the refractive index of the medium according to:

$$n = n_0 + n_2 I \tag{3.8}$$

where I is the applied optical intensity, n_0 is the normal and n_2 is the nonlinear refractive index. The latter index is of the order of $10^{-16} cm^2/W$ for solid state materials and it becomes significant for pulses of high intensity. This technique was initially proposed by the Sibbett group in 1991 and it allows the generation of ultrashort laser pulses with a duration of a few femtoseconds [SKS91].

As seen in the right picture of figure 3.2, a Kerr lens is required at an intracavity focus in the gain medium in order to produce KLM.

An important characteristic of the KLM is that the Kerr medium inside a laser cavity goes through self focussing and self-phase modulation. Self focusing is the nonlinear lensing of the laser pulse arising from the nonlinear refractive index of the Kerr medium. The refractive index changes across the beam profile since the power density distribution in a Gaussian beam is not uniform. At the center of the beam this change is greater compared to its edges and as a result a rod of the active Kerr medium can perform as a lens for high intensity light. More information on the mode locking technique can be found in [SH76] and on the nonlinear optical Kerr-effect in [SKS91].

In order to successfully generate ultrashort laser pulses, the phase relationship between longitudinall modes must be preserved over the whole operation time of the laser so that the mode locking is stable. Therefore, one has to compensate for the dispersive elements inside the cavity. This is the subject of the next section.

3.1.3 Dispersion compensation

It is crucial for the manipulation and the successful utilization of ultrashort pusles that they maintain their temporal shape and their duration whilst propagating through different optical elements. Thus, it is necessary to compensate for the dispersion caused by these media in order to maintain the ultrashort pulses.

The spectral phase of a pulse, $\phi(\omega)$, changes when it propagates through a dispersive element. It can be expanded in a Taylor series around the central pulse frequency ω_0:

$$\phi(\omega) = \phi(\omega_0) + \frac{\partial\phi(\omega)}{\partial\omega}(\omega - \omega_0) + \frac{1}{2}\frac{\partial^2\phi(\omega)}{\partial\omega^2}(\omega - \omega_0)^2 + \mathcal{O}(\omega^3) \quad (3.9)$$

The first three terms correspond to the major effects that contribute to the total dispersion. The first term is the overall phase accumulation arising from the fact that the propagation phase is added to all frequencies. The second term describes the group delay (GD) considering that the whole pulse is delayed compared to a pulse which propagates in free space. The third term is the group delay dispersion (GDD) which is a frequency dependent group delay of the different spectral components of the pulse and causes temporal broadening to the pulse for each round trip through the cavity. In a uniform medium, GDD can be quantified as the GD *dispersion parameter*:

$$D = -\frac{\lambda}{c}\frac{d^2n}{d\lambda^2} \quad (3.10)$$

If $D < 0$ the medium has *positive dispersion* and if $D > 0$ the medium has *negative dispersion*. Higher order terms, for instance of the third-,

fourth- and fifth-order that contribute to the dispersion can be neglected for the moment although they still are some of the limiting factors for shortening the pulse duration. More information about them can be found in [Coj03].

Some of the most efficient dispersion compensation devices include chirped mirrors, pairs of wedges and pairs of prisms. Chirped mirrors are usually coated with a stack of dielectric layers so that different wavelengths can penetrate a different depth of the layer. They are usually used in mode locked lasers with a pulse duration smaller than 20fs. They can simultaneously compensate for GDD and correct for higher order dispersions and they are specified by the amount of negative GDD per bounce they provide. Thus, the compensation is discrete and for further fine-tuning of the dispersion a wedged window pair can be used. Continuous compensation can be achieved since by controlling the insertion of one window, the variable thickness adds a positive GDD in a controlled manner.

Moreover, a prism pair can contribute in geometric dispersions. The prism pair can change the optical path of different frequencies so that all frequencies experience the same cavity round trip time. A prism pair can produce both positive and negative GDD since the relative time delay between the frequencies that it generates can compensate for time delays originating from other dispersive elements. The linear astigmatism introduced by the prisms should also be taken into account and corrected by fine-tuning of the angles of the curved mirrors compensating for all the astigmatism inside the cavity. Finally, most materials introduce a positive dispersion since blue laser light is faster than red. Negative dispersion can be introduced by elongating the optical path of the blue component.

3.2 Ionization in strong laser fields

In this section a general description of the ionization of atoms with strong laser fields will be provided. The main focus will be on the two most significant ionization pictures which are *multiphoton ionization* and *tunnel ionization*. The two different regimes are distinguished by the value of the *Keldysh parameter*.

3.2.1 Multiphoton and tunnel ionization

When the electons of atoms or molecules are exposed to electric fields which are of the same order of magnitude as the fields that bind them to the nucleus, strong field phenomena become present. The first step taking place in these strong physics processes is ionization which in turn leads to other interesting cases, such as high-order harmonic generation [CK07] or above threshold ionization [Ago+79]. The two most significant ionization pictures are *multiphoton ionization*

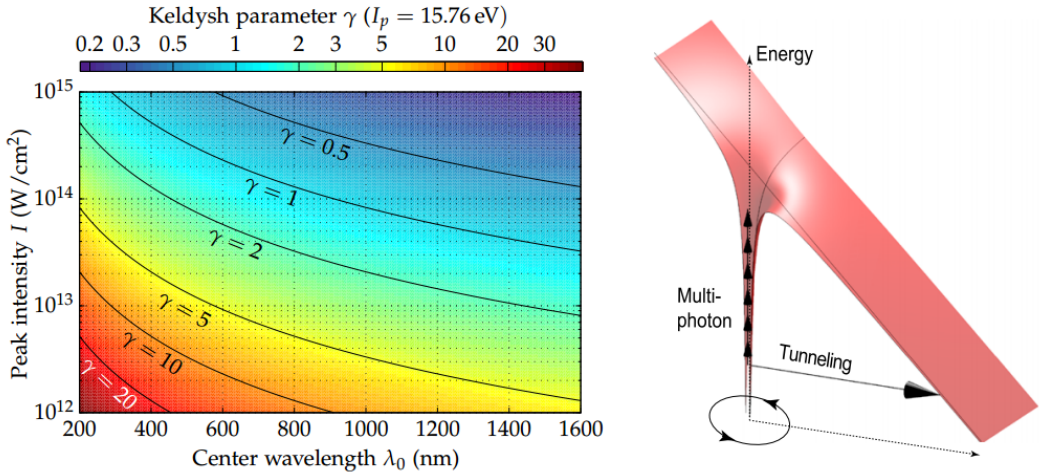

FIGURE 3.3: a) Keldysh parameter for Ar plotted for various wavelengths versus laser intensity. For typical central wavelengths around 780nm and intensities of the order of $10^{14} - 10^{15} W/cm^2$ the Keldysh parameter is $\gamma \sim 1$ [Fec14]. b) Multiphoton and tunnel ionization. The Coulomb field of the atom and the laser field create the combined potential depicted. Ionization can occur either by the multiphoton process or the valence electron can escape by tunneling [LK15].

(MPI) and *tunnel ionization*, as described in p.249 of [LVF86]. Each process is dominating at a different regime which can be indicated from the *Keldysh parameter* [KEL65] given by:

$$\gamma = \omega \frac{\sqrt{2E_i}}{F} = \sqrt{\frac{E_i}{2U_p}} \tag{3.11}$$

where ω is the laser frequency, F is the strength of the electric field, E_i is the ionization potential and U_p is the ponderomotive potential. Equation 3.11 indicates the time that an electron needs in order to tunnel through the barrier compared to the period of the laser field. In case $\gamma \gg 1$ the process is said to be multiphoton ionization, when $\gamma \ll 1$ tunnel ionization dominates, whilst in the case of $\gamma \approx 1$ the system is in an intermediate regime.

The Keldysh parameter can be calculated using formula 3.11 and can be seen in the first picture of figure 3.3 for the case of Ar. γ was calculated for typical laser fields, where the central wavelength is approximately $780nm$ and the peak intensity around $10^{14} - 10^{15} W/cm^2$. The ionization energy of Ar is: $E_i = 15.7596112eV$ [VHU99]. One can see that $\gamma \sim 1$ and both processes are present.

In the right picture of figure 3.3 the two regions of interest are depicted. Multiphoton ionization can be described as a vertical process whilst tunnel ionization as an horizontal process. In the multiphoton region, the electron simultaneously absorbs n photons of low energy in the presence of an oscillating electric field. Therefore, the electron gains enough energy in order to pass the potential barrier. For

higher laser intensities, it is possible that the electron absorbs more photons than it needs for the ionization, leading to a process called *above-threshold ionization* [Ago+79].

Additionally, when the electric field created by the laser is of the order of the electric field of an atomic core, the potential of the atom is modified. This is the tunneling region where the electron tunnels through a potential barrier and has a specific direction of emission which is the one of the instantaneous electric field, i.e. the tunneling barrier is in the direction of the laser electric field. After tunneling most theoretical models assume that the electron is at rest. Tunneling ionization is sufficient to describe the majority of phenomena that take place in strong field physics.

For the mathematical description of those two regimes low order time-dependent perturbation theory is not possile and other techniques have to be applied. A suitable model for the calculation of the ionization rate in this regime is the *ADK model* which depends on the laser field intensity and was proposed by Ammosov, Delone and Krainov in [ADK86].

3.2.2 The ADK theory

The most widely used models for calculating ionization rates are the *ADK model* [ADK86] and the molecular ADK model [TZL02], which fit quite well the experimental data for noble gases and small molecules [Wal+94]. In the ADK theory the ionization rate depends on the ionization potential of the atom. In 1986, Ammosov, Delone and Krainov published a formula for the ionization rate for complex atoms when the light is linearly polarized and the intensity of the fields in not too strong:

$$\Gamma = C_{n^*l}^2 \, f(l,m) \, \mathcal{E}_0 \sqrt{\frac{3E}{\pi (2\mathcal{E}_0)^{3/2}}} \left(\frac{2}{E} (2\mathcal{E}_0)^{3/2} \right)^{2n^* - |m| - 1} exp\left(-\frac{2(2\mathcal{E}_0)^{3/2}}{3E} \right) \tag{3.12}$$

where

$$C_{n^*l} = \left(\frac{2e}{n^*}\right)^{n^*} (2\pi n^*)^{-1/2} \quad and \quad f(l,m) = \frac{(2l+1)(l+|m|)!}{2^{|m|}\,|m|!(l-|m|)!}$$

and $n^* = Z/\sqrt{2\mathcal{E}_0}$ is the effective principal quantum number, $\mathcal{E}_0$ is the electric binding energy, l is the angular quantum number, m is the magnetic quantum number and e is the Euler-constant. For $l = 1$ we obtain:

$$\frac{\Gamma_{m=0}}{\Gamma_{|m|=1}} = \frac{2}{F} (2\mathcal{E}_0)^{3/2} \gg 1 \tag{3.13}$$

Equation 3.13 indicates that an electron will most probably tunnel from the $m = 0$ orbital rather than the $m = 1$ orbital. For instance, for a neon atom this ratio is approximately equal to 30 in the presence of a laser field of intensity $5 \cdot 10^{14} W/cm^2$ [WC11]. This result is very important for the realization of a *spin-orbit wave packet* in singly charged argon ions and will be discussed in the next section.

3.3 The spin-orbit wave packet (SOWP)

A *spin-orbit wave packet* (SOWP) can be described as the coherent superposition of two electronic states. With the *spin-orbit* we are referring to the coupling between the orbital angular momentum l and the spin s. The orbital angular momenta of the individual electrons are coupled to give a total angular momenum of $\mathbf{L} = \sum_i \mathbf{l}_i$ and likewise the spins of the indivdual electrons are coupled to give a total spin of $\mathbf{S} = \sum_i \mathbf{s}_i$. When the vectors **L** and **S** couple, they give rise to the total angular momentum $\mathbf{J} = \mathbf{L} + \mathbf{S}$. The spin-orbit interaction can lift the degeneracy of the energy levels in atoms, molecules or solids. A spin-degenerate level can be split into energy levels which have a spin parallel or antiparallel to the orbit. An analytical description of the *LS or Russell-Saunders coupling* can be found in various textbooks like for example in Chapter 10 of [Dra06].

The dynamics of a wave packet can be studied in pump-probe experiments where two ultrashort laser pulses are utilized. Initially, the energetic levels of the atom are coupled. The first laser pulse, i.e. the pump pulse, ionizes the neutral atom from the p orbital aligned along the polarization axis of the laser pulse and creates the wave packet in the ion. The interaction of the atom with the external laser field lifts the degeneracy of the energetic states and the latter become uncoupled. The wave packet is created by the coherent superposition of the two uncoupled states. Then a second laser pulse probes the wave packet to a final state which can be detected by time-independent methods. In order to observe the dynamics of the system it is necessary that the probability to find the system in a specific state varies with time.

For the mathematical description of a SOWP in noble gases, which is the case of our interest, we follow the description from Chapter 5 of [Fec14] and [Wen+06] will be followed. Atomic units will be used throughout this analysis. The Hamiltonian of the electron including a kinetic term and a Coulomb potential is $H = p^2/2 - 1/r$ and the eigenstates of the system will be represented by $\psi_{n,l,m}$. During the analysis we will work on both the *uncoupled* and the *coupled* basis, where for the former the tunnel ionization rate depends on l and m and for the latter the equations depend on J and m_J, where m_J is

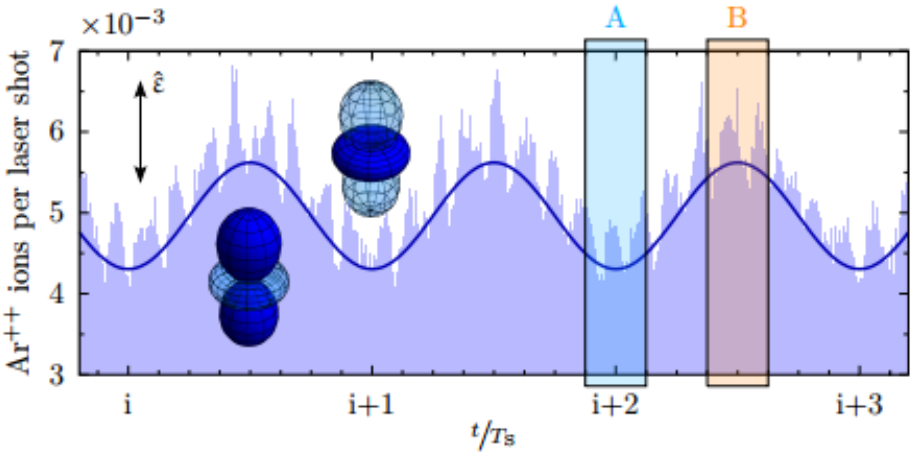

FIGURE 3.4: Characteristic fingerprint of a SOWP in Ar^+. The ionization of an electron from the m=0 orbital is favored as indicated by the inset orbitals. The data have been fitted by a sine function [Fec+14].

projection quantum number of the total angular momentum J. Initially, when the system is in the ground state, the *coupled* basis will be utilized for its description:

$$\Phi(t=0) = \sqrt{\frac{2}{3}}\psi_{\frac{3}{2},\frac{1}{2}} - \sqrt{\frac{1}{3}}\psi_{\frac{1}{2},\frac{1}{2}} \tag{3.14}$$

where the notation for the wave function is ψ_{J,m_j}. The SOWP is formed by the linear combination of its two lowest spin-orbit states given by 3.14.

When the atom interacts with a strong laser field only the spatial part of the wave function is affected since the intensity of the laser is in the nonrelativisitc regime. This interaction leads to an electronic transition to a specific excited state. For the evolution of the system the time evolution operator needs to be implemented, $\hat{T} = exp(-i\hat{H}t)$:

$$\Phi(t) = \sqrt{\frac{2}{3}}e^{-i\omega_{3/2}t}\psi_{\frac{3}{2},\frac{1}{2}} - \sqrt{\frac{1}{3}}e^{-i\omega_{1/2}t}\psi_{\frac{1}{2},\frac{1}{2}} \tag{3.15}$$

where $\omega_{3/2}$ and $\omega_{1/2}$ are the energies corresponding to the eigenstates $\psi_{3/2,\pm1/2}$ and $\psi_{1/2,\pm1/2}$ respectively. Equation 3.15 can be written in the *uncoupled* basis, ψ_{l,m,m_s}:

$$\Phi(t) = \frac{\sqrt{2}}{3}(e^{-i\omega_{3/2}t} - e^{-i\omega_{1/2}t})\psi_{1,1,-1/2} + (\frac{2}{3}e^{-i\omega_{3/2}t} + \frac{1}{3}e^{-i\omega_{1/2}t})\psi_{1,0,1/2} \tag{3.16}$$

The probabilities to find the system in the state for which $m = 0$ or $|m| = 1$ can be seen in figure 3.4 and when calculated give:

$$P_{m=0}(t) = \frac{5}{9} + \frac{4}{9}cos(\Delta\omega t)$$

$$P_{|m|=1}(t) = \frac{4}{9}[1 - cos(\Delta\omega t)] \tag{3.17}$$

where $\Delta\omega = \omega_{3/2} - \omega_{1/2}$ is the energy difference between the two states. According to [Wen+06], 89% of the population oscillates between $^2P_{3/2}$ and $^2P_{1/2}$ with a characteristic period of:

$$T_S = 2\pi/\Delta\omega. \tag{3.18}$$

In the case of singly charged argon the spin-orbit splitting is $177.5meV$ and thus the period of the SOWP is $23.3fs$ [KRR13]. Also, in section 3.2.2 we saw that ionization from the $m = 0$ orbital is much more probable than from the $|m| = 1$ orbital. In the case of singly charged argon and for laser intensities of $10^{14} - 10^{15}W/cm^2$ the ratio of equation 3.13 is from 15 to 47 for Ar and 34 to 108 for Ar^+ [Fec14]. The ionized electron can be treated as a 'hole' which will justify the mathematical treatment that has been followed, as proposed by [RS09] and [WC11].

Finally, it is clear that an accurate technique must be implemented in order to achieve the high resolution required to observe an isotopic shift in singly charged argon. The technique used for the purpose of this experiment is Ramsey-like spectroscopy where two strong and ultrashort laser pulses were utilized in order to observe the shift. The first pulse was used to create a coherent superposition of the two states where the SOWP has a beating period of approximately $23fs$. The second pulse probes the system after a delay of $\sim 3ns$. This pump-probe scheme was applied on an argon gas jet containing the different isotopes and those were differentiated through mass spectrometry in our spectrometer chamber, a Reaction Microscope. The next chapter consists of a brief description of the Ramsey scheme as well as the experimental setup utilized for the realization of this experiment.

Chapter 4

Spectroscopic technique and experimental setup

4.1 Spectroscopic technique

Ramsey spectroscopy or alternatively known as the *separated oscillating fields method* is a form of interferometry initially proposed by N. Ramsey in 1949 [Ram50]. It measures the transition frequencies in atoms by taking into account the phenomenon of magnetic resonance. This technique follows the idea of I. I. Rabi who developed a method for measuring the frequency of an atomic transition [Rab+38]. This method will be described in the first part of this chapter together with Ramsey spectroscopy which will be reviewed in more detail. The second part of this chapter is about the experimental apparatus utilized in order to measure the isotopic shift between ^{40}Ar and ^{36}Ar, consisting of the femtosecond laser system, a Mach-Zehnder interferometer and the Reaction Microscope (ReMi).

4.1.1 Rabi oscillations

For the description of Rabi oscillations we will consider a two-level system which interacts with weak harmonic classical radiation. The ground state $|g\rangle$ of the system and the excited state $|e\rangle$ are separated with a transition frequency $\omega_0 = (E_e - E_g)/\hbar$. A harmonic radiation of the form $\mathbf{E}(t) = \mathbf{E}_0\ cos(\omega t)$ is applied to the system with a frequency ω, chosen such that it is close to the resonance $\mid \omega - \omega_0 \mid \ll \omega_0$. The two-level Hamiltonian, as seen in Chapter 9 of [Ban06] for instance, is given by:

$$\hat{H} = -\frac{\omega_0}{2}\sigma_z - Acos(\omega t)\sigma_x \tag{4.1}$$

where $\sigma_x = \begin{pmatrix} 0 & 1 \\ 1 & 0 \end{pmatrix}$ and $\sigma_z = \begin{pmatrix} 1 & 0 \\ 0 & -1 \end{pmatrix}$ are the Pauli matrices and $A = \langle e| \hat{\mathbf{d}} \cdot \mathbf{E}_0 |g\rangle$, where $\hat{\mathbf{d}}$ is the dipole moment operator. An Ansatz for the wavefunction of the system is:

$$|\Psi(t)\rangle = C_g(t)e^{-iE_g t}|g\rangle + C_e(t)e^{-iE_e t/}|e\rangle \tag{4.2}$$

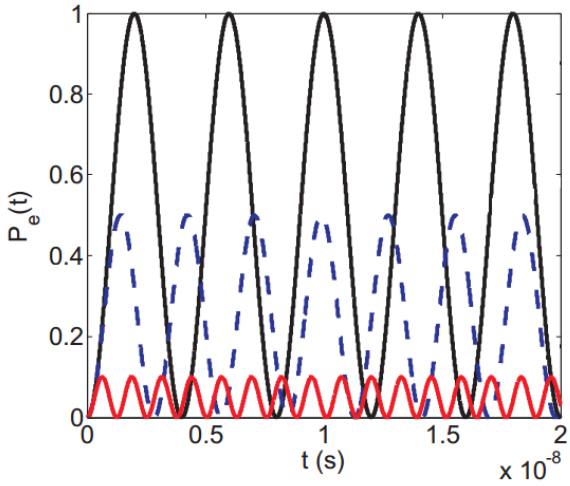

FIGURE 4.1: Rabi oscillations. A two-level system interacts with a weak harmonic radiation. The blue dashed plot and the red plot depict the probability for different values of the detuning $\Delta/2\pi = (\omega - \omega_0)/2\pi$. The value for the blue dashed plot is $\hbar\Delta/A = 1$ and for the red dashed plot $\hbar\Delta/A = 3$. The figure is taken from [Bj1].

with $E_g = -\omega_0/2$ and $E_e = \omega_0/2$. From the Schrödinger equation we obtain an expression for the coeffecients:

$$\dot{C}_g = iAcos(\omega t)e^{-i\omega_0 t}C_e$$
$$\dot{C}_e = iAcos(\omega t)e^{i\omega_0 t}C_g \tag{4.3}$$

By using the *Rotating Wave Approximation* (in which rapidly oscillating terms are neglected) and applying the initial condition $C_g(0) = 1$ and $C_e(0) = 0$, the solution to the system described by 4.3 is:

$$C_e(t) = i\frac{A}{\Omega_R}e^{i\Delta t/2}sin(\Omega_R t/2)$$
$$C_g(t) = e^{-i\Delta t/2}(cos(\Omega_R t/2) + i\frac{\Delta}{\Omega_R}sin(\Omega_R t/2)) \tag{4.4}$$

where $\Omega_R = \sqrt{\Delta^2 + A^2}$ is the *Rabi frequency* and $\Delta = \omega - \omega_0$ is the detuning. The initial condition indicates that the system initially occupies the ground state. The probabilities to find the system either in state $|e\rangle$ or in state $|g\rangle$ are obtained by squaring the coefficients of 4.4 respectively. For instance, the probability to find the system in the excited state is:

$$P_e(t) = |C_e(t)|^2 = \frac{A^2}{\Omega_R^2}sin(\omega_R t/2)^2 \tag{4.5}$$

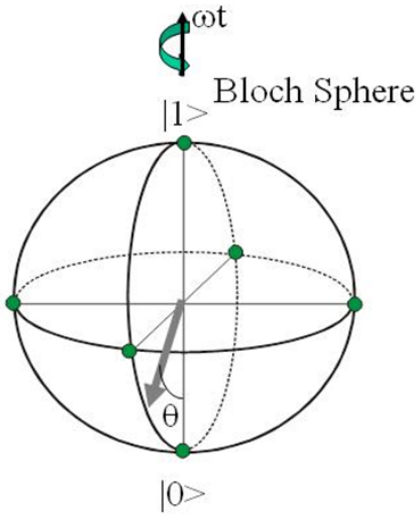

FIGURE 4.2: Bloch sphere representation of the Rabi oscillations. By applying a π pulse to the two-level system can result in a complete transfer of population from one state $|0\rangle$ to another $|1\rangle$. The pseudo-spin vector initially points towards the south pole of the sphere and then it evolves until it reaches the north pole.

This probability can be seen in figure 4.1 plotted for different driving frequencies. The detuning between the harmonic radiation frequency and the frequency of the atomic transition varies between 0 and $750MHz$.

An alternative way to describe Rabi oscillations is by using the Bloch sphere representation as depicted in figure 4.2. The Bloch sphere is a geometrical representation of a two level system for which the north and the south pole are typically chosen to correspond to spin-up and spin-down states of the electron. In this 2-sphere, if a pulse of duration $\tau_\pi = \pi/\Omega_R$, namely a π-pulse, is applied to the two level system then its population will be transfered from the ground state $|g\rangle$ to the excited state $|e\rangle$. A π-pulse can swap the two states of the system in a superposition [Foo05]:

$$c_1 |g\rangle + c_2 |e\rangle \rightarrow -i[c_1 |e\rangle + c_2 |g\rangle] \tag{4.6}$$

4.1.2 Ramsey spectroscopy

As the name suggests, Ramsey spectroscopy was developed by N. F. Ramsey for which he won the Nobel prize in 1989 [Ram90]. It is based upon Rabi's method but instead of applying a single coherent field over a total time T, two oscillatory fields are used. Each one of them has a short duration τ which is separated by a time T where there no field is present. This technique can be successfully used for both atomic and molecular beam experiments which interact with external fields. One of the most significant applications of

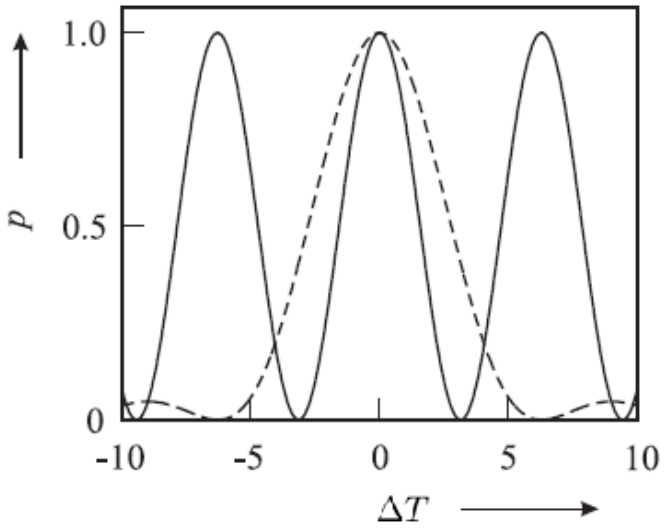

FIGURE 4.3: A comparison between the Rabi and the Ramsey method. The probability to find the two-level system in the excited state is almost twice when using two $\pi/2$ pulses separated by a region where the presence of the field is zero. The solid line referrs to the Ramsey scheme and the dashed one to the Rabi scheme. The picture is adapted from [Ram90].

this process is the caesium atomic clock and subsequently the precise determination of the second.

A brief mathematical description of the Ramsey method, following [Ram56], is essential for a deeper understading of this scheme. In the previous analysis, equations 4.4 were referring to the probability amplitudes of finding the two-level systen either in the ground or in the excited state. It was assumed, by the conditions $C_g(0) = 1$ and $C_e(0) = 0$, that the system was in the ground state just before the interaction with the weak field took place. A more general expression must be evaluated for the case of two oscillating fields interrupted by a free field for time T. The two-level system at the beginning of the interaction is described by the probability amplitudes $C_g(t_1)$ and $C_e(t_1)$ respectively. The new probability amplitudes will be of the form $C_g(t_1+t)$ and $C_e(t_1+t)$ for an interaction starting at t_1 and evolving until $t_1 + t$. The first term gives the probability that the systen is in the ground state after the first interaction and gets excited during the second interaction. The second term gives the probability of finding the system in the excited state after the first interaction takes place and entering the second interaction in this state. By summing those two contribution the probability amplitude of finding the atom in the excited state after the second interaction with the field can be evaluated. Ramsey's calculation leads to:

$$p(\tau + T + \tau) \equiv | C_e(\tau + T + \tau) |^2 =$$

$$= 4\frac{A^2}{{\Omega_R}^2} sin^2 \frac{\Omega_R \tau}{2} \Big(cos\frac{\Omega_R \tau}{2} cos\frac{\Delta T}{2} - \frac{\Delta}{\Omega_R} sin\frac{\Omega_R \tau}{2} sin\frac{\Delta T}{2} \Big)^2 \qquad (4.7)$$

Close to resonance, where the the conditions $\Delta \ll A$ and $\Omega_R \cong A$ apply, equation 4.7 becomes:

$$p(\tau + T + \tau) \approx \frac{1}{2} sin^2 \Omega_r \tau [1 + cos 2\pi(\omega - \omega_0)T] \qquad (4.8)$$

From equation 4.8, the probability of finding the system in the excited state after the second interaction with the field maximizes for $\tau_\pi = \pi/2\Omega_R$, namely for $\pi/2$ pulses. Since the FWHM is given by $\Delta\omega = 1/2T$, the advantage of the Ramsey method over the Rabi is obvious since the probability of excitation of the system is about twice that of the former case as seen in figure 4.3. This advantage is profound for the case when the total interaction time is the same for the two methods.

When applying this method to an experiment, the interaction of the system studied with the two phase coherent fields originating from the same source must be taken into account. A phase difference $\Delta\phi$ between the first and the second zone of the system must be added to equation 4.8:

$$p(\tau + T + \tau) \approx \frac{1}{2} sin^2 \Omega_r \tau [1 + cos 2\pi(\omega - \omega_0)T + \Delta\phi] \qquad (4.9)$$

As a result, when high accuracy is required this phase must be kept as low and as constant as possible. If frequency shifts result from varying this phase then the advantages of using two oscillatory fields compared to a continuous interaction zone are obvious. This occurs as the phase can be controlled more precisely in the case of a limited interaction region compared to an extended region.

The Bloch sphere representation can be utilized once again for the study of the two-level system as seen in figure 4.4. During a pulse sequence the evolution of the density operator will be represented by the Bloch vector. In this pseudo-spin picture two short coherent pulses of duration τ are separated by an interaction region with an adjustable duration T. Initially, the system is prepared in the ground state $|g\rangle$ with the pseudo-spin vector pointing towards the south pole of the Bloch sphere as seen in picture 4.4 a). A $\pi/2$-pulse of short duration rotates the pseudo-spin by an angle of $\theta = \pi/2$ and excites it to the equatorial plane. In the Ramsey scheme the pulses are considered instantaneous and therefore imperfections such as population losses and dephasing can be neglected. For the coupling, it is necessary that the Rabi frequency is much greater than the detuning, i.e. $\Omega_R \gg \Delta$. After the first $\pi/2$-pulse, the system is freely evolving

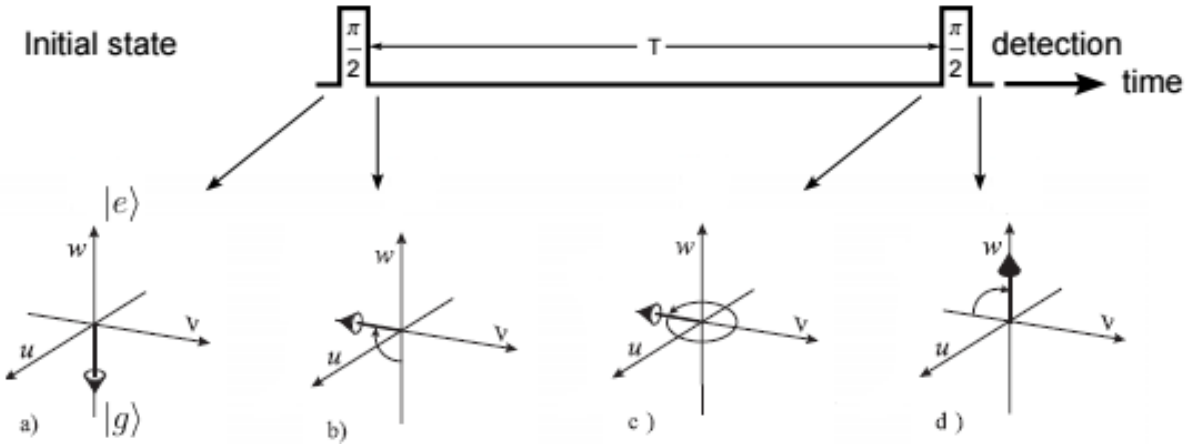

FIGURE 4.4: Lossless evolution of the pseudo-spin (Bloch vectror) after the interaction with two short $\pi/2$-pulses separated by a delay T. a) The system is prepared in the ground state, i.e. the pseudo-spin vector is pointing on the south pole of the Bloch sphere. b) A short $\pi/2$ pulse is applied to the system exciting it in the u-v plane. c) The system evolves for time T whilst the pseudo-spin performs several cycles on the equatorial plane. d) If a second short $\pi/2$-pulse is applied to the system, after it has evolved for an even number of cycles, it excites the population to $|e\rangle$. The figure is adapted from [Iva13] and [Rie06].

and there is no interaction with an external field since the latter has been switched off. The pseudo-spin rotates in the equatorial plane as seen in figure 4.4 c). The ground $|g\rangle$ and the excited state $|e\rangle$ are *clock states*, i.e. they are dynamical states separated by constant time intervals. They are used to control the duration of a process like for instance the precession of a spin in a magnetic field. Finally, a second $\pi/2$-pulse can further excite the system and bring the pseudo-spin pointing towards the north pole of the Bloch sphere as seen in figure 4.4 d). This can occur when the time delay is such that the pseudo-spin has performed an even number of cycles on the equatorial plane, i.e. the angle of rotation is $2\pi n$. Otherwise, the second pulse will not change the orientation of the Bloch vector or it will direct it in a different position. If the probability of finding the system in the excited state is plotted, it will have a sinusoidal form as a function of $2\pi(\omega - \omega_0)T$. Within the Ramsey scheme the difference between the phase of the external oscillating field $2\pi\omega T$ and the the phase of the quantum system $2\pi\omega_0 T$ can be measured.

The main advantage of the Ramsey method, compared to applying a continuous coherent field, is that the accuracy of the measurement is significantly improved. By extending the time delay the precision of a measurement can be significantly increased. This occurs since the measuring value increases during the interrogation time T whilst the value of the error stays the same. This high accuracy is necessary for the detection of such a small energy difference as the isotopic shift between ^{40}Ar and ^{36}Ar.

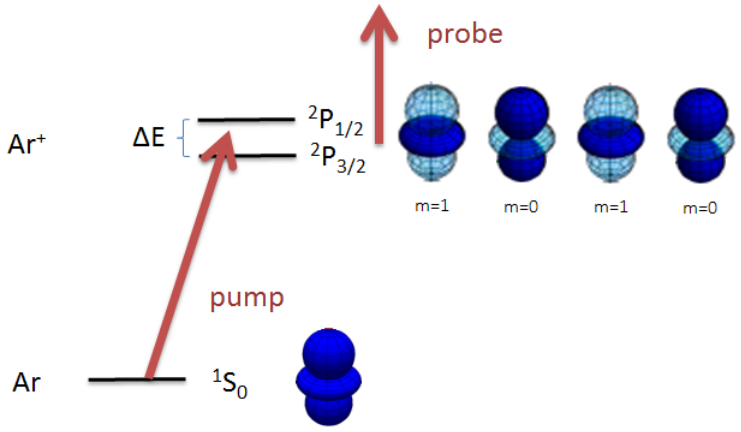

FIGURE 4.5: Applying the Ramsey scheme in this experiment. The atomic transition studied is the $3s^2 3p^5$ ($^2P_{3/2} \rightarrow {}^2P_{1/2}$). An ultrashort pump beam creates the SOWP, i.e. a coherent superposition of the $^2P_{3/2}$ and $^2P_{1/2}$ states in singly charged argon ions. A second time delayed ultrashort laser pulse further probes the dynamics of the system. The SOWP is ignited in the m=0 orbital of the valence shell of argon.

4.1.3 Creating a spin-orbit wave packet

We implemented a Ramsey-like scheme in our experiment. We studied the transition $3s^2 3p^5$ ($^2P_{3/2} \rightarrow {}^2P_{1/2}$) for singly ionized argon atoms by using two ultra-short ($\sim$ 6fs) laser pulses. The first laser pulse excites the system in a coherent superposition of the aforementioned states. This superposition leads to a spin-orbit wave packet whose dynamics can be investigated by applying a second delayed probe pulse.

Initially, the system is prepared in the ground state of the neutral atom. The first ultrashort laser beam, i.e. the pump beam, excites the system and it creates a superposition of the $^2P_{3/2}$ and $^2P_{1/2}$ states, as seen in figure 4.5. This pump pulse removes an electron from the atomic p-shell which can alternatively be seen as a 'hole' in the valence shell. The electron is most likely removed from the $m = 0$ orbital aligned along the laser pulse. The energy separation of those two states is $\sim 0.18eV$ which corresponds to a period of $\sim 23.3fs$. The superposition of those two states in the Ar^+ ion, i.e. the SOWP, oscillates with this period. According to [Fle+11], the wave packet can oscillate for relatively long times, on the order of at least a few ns or even longer, since there are no decay channels present. Another ultrashort laser pulse, i.e. a probe pulse, is applied after a delay on the order of ns. With this second pulse one can further investigate the dynamics of the system. By controlling the time delay between the two ultrashort laser pulses the relative contributions from the two states can be controlled.

4.2 Experimental setup

The experimental apparatus used for measuring the isotopic shift between ^{40}Ar and ^{36}Ar consists of three main parts, the femtosecond laser system, the Mach-Zehnder interferometer and the Reaction Microscope (ReMi).

The need to investigate phenomena in such short time scales requires the use of laser pulses of short durations and high intensities. The generation of ultrashort laser pulses is accomplished with a commercial femtosecond laser system. These pulses, however, require further modifications in order to achieve the desired duration and compensate for dispersion induced by the laser system. The second part of the setup consists of a Mach-Zehnder interferometer necessary for performing pump-probe experiments. It consists of two beam splitters (BS), where the first one splits the incoming laser beam into a pump pulse and a time-delayed probe pulse. The two pulses meet again on the second beam splitter and they are guided to the Reaction Microscope. Inside the ReMi the laser beam interacts with a gas jet of atoms and the products of this reaction can be detected.

4.2.1 The femtosecond laser system

For this experiment a commercial *FEMTOLASERS* "FEMTOPOWER compact PRO HP/HR" Ti:Sapphire (Ti:Sa) laser system was used. More information about it can be found in [Gmb06] and [Gmb] whilst general information on Ti:Sa lasers can be retrieved from section 6.7.2 of [DR06]. The system consists of three major parts, the oscillator, the amplifier and the compressor as can be seen in figure 4.6.

The oscillator consists of a continuous wave (cw) mode-locked neodymium-doped yttrium orthovanadate (Nd:YVO) system which is used to produce the ultrashort laser pulses by pumping a Ti:Sa crystal. The central wavelength of this green laser beam is $532nm$. The output power is $3W$ and the pulses produced are close to being Fourier limited with a duration of less than $10fs$. KLM ensures the creation of ultrashort laser pulses since the adjacent cavity modes are locked as explained in section 3.1.2. The repetition rate at this point is $80MHz$ resulting in a low output energy of approximately $1nJ$. A set of stretchers is placed after the oscillator in order to elongate the beam duration and reduce the peak energy of the pulses. The pulse is temporally stretched and passes nine times through the gain medium which is a Ti:Sa crystal. The laser spectrum after the oscillator can be seen in figure 4.7. The high peak at $532nm$ comes from the pump laser. During the context of this thesis the oscillator went frequently out of mode-lock.

The next part of the femtosecond laser system is the amplifier which is necessary in order to increase the pulse energy of the output beam. After the oscillator the pulse has an energy of $\sim 1nJ$ which

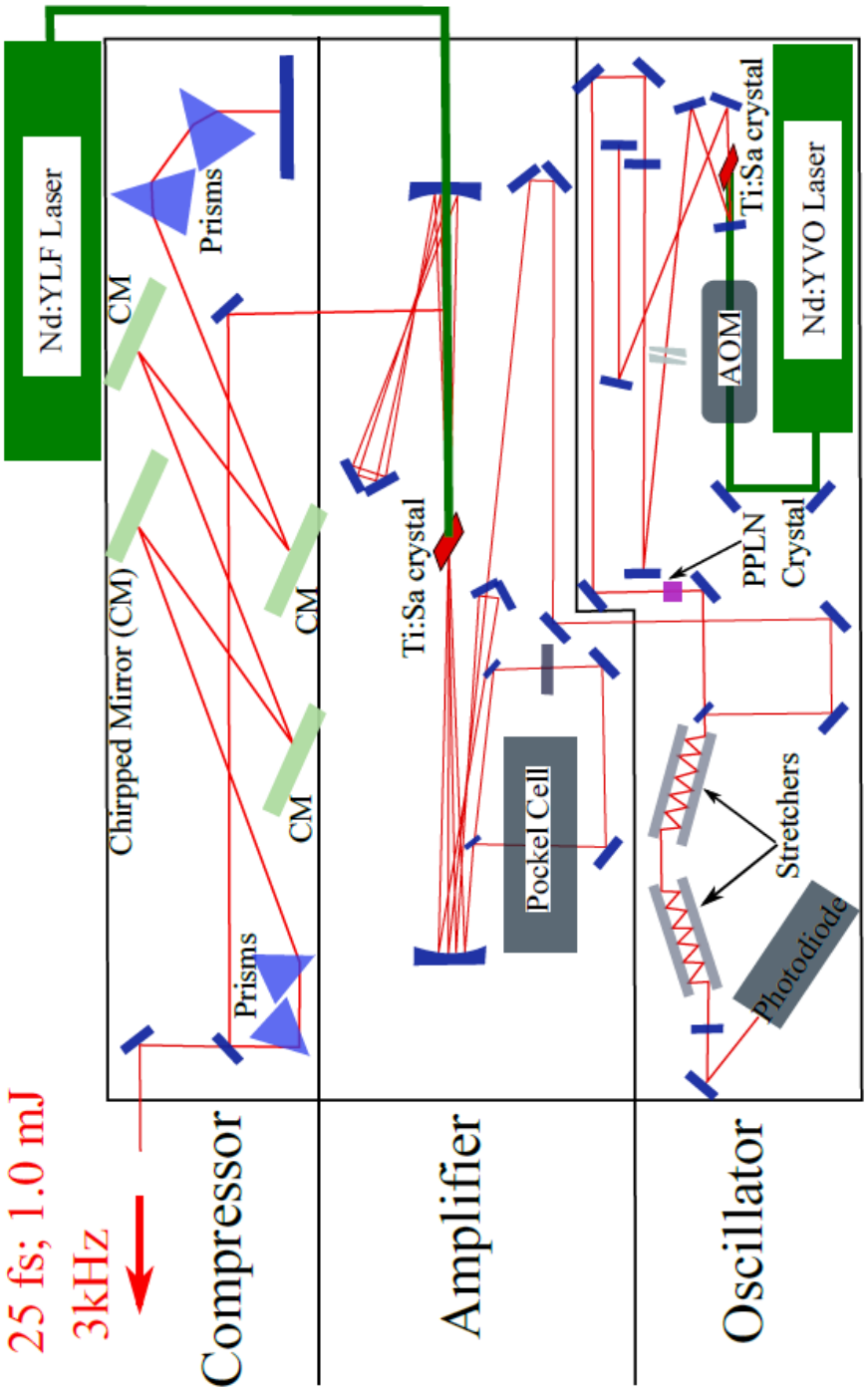

FIGURE 4.6: The femtosecond laser system. It consists of three main parts, the oscillator, the amplifier and the compressor. It produces ultrashort ($25fs$) and intense ($10^{14}W/cm^2$) laser pulses, has an output energy of $1.0mJ$ and a repetition rate of $3kHz$.

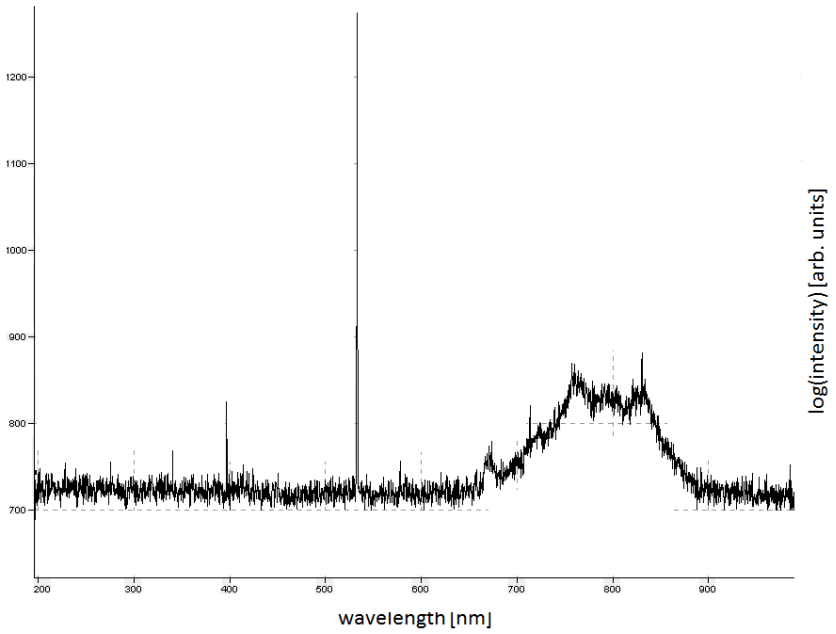

FIGURE 4.7: Laser spectrum after the oscillator. The high peak originates from the pump laser.

is not sufficient to ionize atoms. The amplification occurs by focusing the pulses on a second Ti:Sa crystal in a *chirped pulse amplification* scheme which increases their energy by a factor of one million [SM85]. They pass through the Ti:Sa crystal nine times in total and after the forth time they travel through a Pockel cell. They turn the polarization for every 10.000th laser pulse such that a particular pulse can travel through a subsequent polarization filter. After the Pockel cell the repetition rate has decreased from 80MHz to 3kHz.

The third part of the femtosecond laser system is the compressor. As the name suggests, the pulses at this stage are temporally compressed in order to achieve the desirable pulse duration. A set of optical prisms and chirped mirrors provide a negative refraction index and correct for higher orders of dispersion as explained in section 3.1.3. The laser pulses emerging after the compressor part have a duration of approximately $25fs$, an energy of $1.0mJ$ and a repetition rate of $3kHz$. Those properties are compared for the three different parts of the femtosecond laser system as seen in table 4.1. Initially, pulses of short duration are produced ($\leq 10fs$) whilst after the compressor their duration has increased since the bandwidth has been effectively reduced. Also, the output power is increased making ionization possible. This reduction of the spectral width during the amplification process must be compensated in order to produce ultrashort laser pulses. For this, the implementation of the nonlinear optical effect called *self-phase modulation* (SPM) is required.

pulse characteristics	**oscillator**	**amplifier**	**compressor**
pulse duration	¡10fs	300ns	25fs
central wavelength	532nm	527nm	780nm
repetition rate	80MHz	3kHz	3kHz
average power	80mW	10W	3W
pulse energy	1.0nJ	$\sim$ 3.33mJ	1.0mJ

TABLE 4.1: Characteristics of the laser pulses at the three different parts of the femtosecond laser system.

4.2.2 Setup for the generation of few-cycle pulses

As a pulse propagates through a dispersive medium no new frequencies are generated. However, if the medium is nonlinear, different frequencies will superpose with different phases leading to a distortion of the shape of the pulse and eventually to the generation of new frequencies according to Chapter 8.4 of [Gha11]. The refractive index of a material for large intensities was given in equation 3.8. The change of the refractive index with intensity results in a shift in the instantaneous phase of the pulse:

$$\phi(t) = \omega_0 t - \frac{2\pi}{\lambda_0} n(I) L \tag{4.10}$$

where L is the distance that the pulse has propagated. The phase shift of the pulse produces a frequency shift where the *instantaneous frequency* is given by:

$$\omega(t) = \frac{d\phi(t)}{dt} = \omega_0 - \frac{2\pi L}{\lambda_0} \frac{dn(I)}{dt} \tag{4.11}$$

Due to SPM, the instantaneous frequency $\omega(t)$ within the pulse changes with time and the pulse is chirped. The frequency shift of each part of the pulse can be seen by plotting $\omega(t)$. The leading edge of the pulse shifts towards lower values of the frequency whilst the trailing edge towards higher frequency values. The peak of the pulse stays the same and the temporal shape does not change. Due to this effect, dispersion is increased and thus the pulse is positively chirped and its spectrum is broadened leading to the generation of shorter laser pulses.

The hollow-core fiber

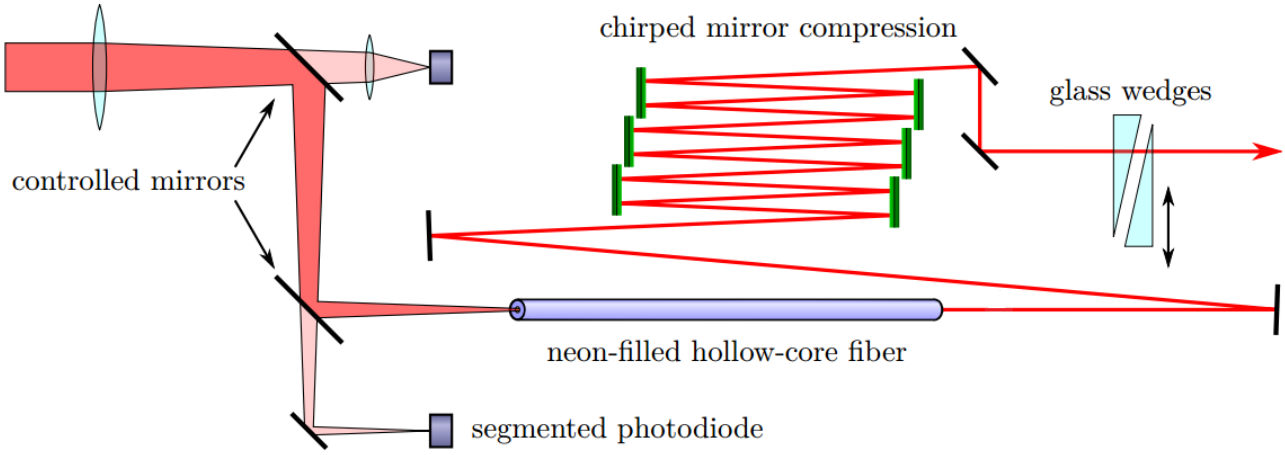

FIGURE 4.8: Experimental setup utilized for the generation of few-cycle pulses. After the femtosecond laser system, the beam is focused onto a hollow-core fiber filled with neon gas. Fiber coupling is achieved with the help of two controlling mirrors and stabilized with a segmented photodiode. The shortened pulses are temporally compressed as they are reflected from three pairs of chirped mirrors. A pair of glass of wedges ensures fine-adjustment of the overall dispersion and further shortens the duration of the pulses. The figure is adapted from [Fec14].

The femtosecond laser setup delivers ultrashort laser pulses with a duration of $25fs$. However, since even shorter pulses are required for this experiment, they are focused onto a hollow-core glass fiber filled with neon gas with 3 bars of pressure. A lens with a focusing length of approximately 1.5m focuses the beam to the center of the fiber. The single-mode fiber has a length of about 1m and a diameter of 250μm and can select only the zeroth mode of the Gaussian beam. When the beam propagates through the fiber it interacts with the neon atoms which act as the nonlinear medium required for the SPM process. Thus, further dispersion is introduced into the system. The spectral width of the beam is broadened, allowing for the production of even shorter pulses. The central wavelength is reduced from 780nm to 740nm. This part of setup can be seen in figure 4.8. Proper fiber coupling is essential both for gaining the maximum output power after the fiber as well as for not destroying it during alignment. The beam is focused onto the fiber with the help of a pair of mirrors. One of them is connected with a controller which provides μm accuracy and the second one is controlled by hand. A segmented photodiode compensates for spatial drifts of the laser beam which can take place during a measurement ensuring optimal and stable incoupling into the fiber for long measuring times. The photodiode is divided in a four-fold region where a small part of the beam is focused and small drifts can be detected and compensated. Stabilization over long periods of time is ensured since the photodiode is connected to a computer and controlled by a LabVIEW program.

Pulse compression after the fiber

After propagating through the hollow-core fiber, the pulses have significantly reduced their duration or alternatively have gained a very broad spectrum. This broad spectrum is quite sensitive to dispersion. As explained in section 3.1.3 when a pulse travels through different optical media and air, the different frequencies in the pulse create an individual phase. Pairs of *chirped mirrors* can be used to compensate for this effect by introducing negative dispersion. These multi-layer mirrors allow specific wavelengths to penetrate at different depths and more specifically red components can penetrate deeper into the mirror and travel longer distances compared to the blue components. In the experiment, the red frequencies have to be delayed relative to the blue components since they propagate faster than the latter ones. Three pairs of chirped mirrors were used and the laser pulses hit each mirror twice resulting in twelve reflections in total. The mirrors are designed in such a way that they temporally recompress the beam to its minimal time duration without changing its spectral profile. A pair of wedges is placed after the mirrors for fine adjustment of the total dispersion. The duration of the pulses delivered after the pair of wedges was measured to be around 6fs. More information about the pulse duration and the way it can be measured can be found in [Fec14] and [Cam13].

4.2.3 The Mach-Zehnder interferometer

The Mach-Zehnder interferometer is based on the interference of two beams by splitting the amplitude of the incoming wave. With this setup the relative phase shift variations between two beams caused by a change in length of one of the paths can be determined. As the name of this type of interferometer suggests, Zehnder proposed this configuration in 1891 [Zeh91] and since then it has been continuously utilized in pump-probe measurements. More details concerning this setup can be found in Chapter 4.2.3 of [Dem13].

In this experiment two pulses are required separated by a time delay with respect to each other for the observation of the isotopic shift between ^{40}Ar and ^{36}Ar. The first pulse, i.e. the pump pulse, creates a coherent superpostion of the $^2P_{3/2}$ and $^2P_{1/2}$ states. This is the SOWP which has been already described in section 3.3. The second pulse is applied to the system after a time delay in order to probe its dynamics. During this time delay the system evolves freely. Initially, the pulse propagates through a 50/50 beam splitter (BS) which creates two identical beams which travel through the two arms of the interferometer. Both arms consist of a set of two mirrors. The second arm of the interferometer has been moved by $(119.0 \pm 2.0)cm$ away from the first arm which means that a delay of $(3.97 \pm 0.07)ns$ has

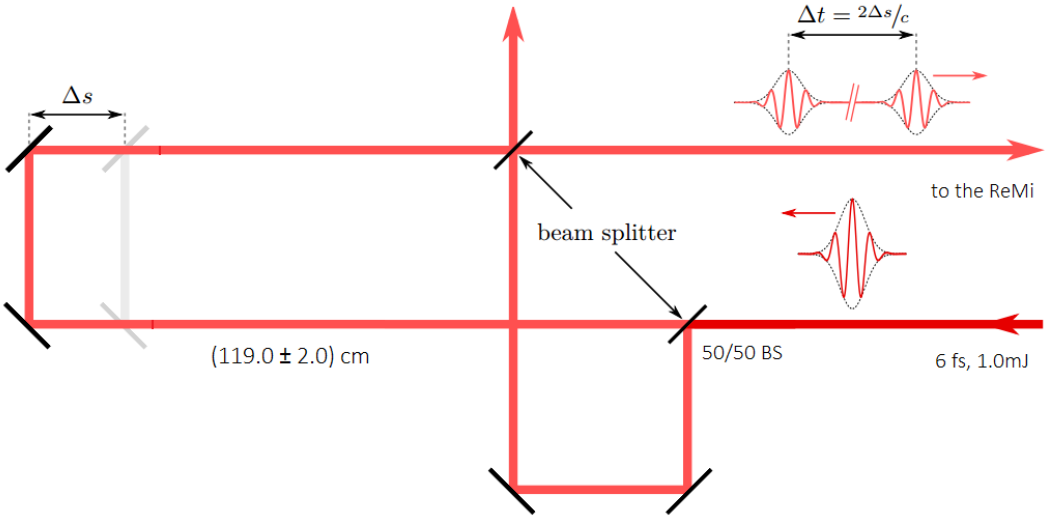

FIGURE 4.9: The Mach-Zehnder interferometer. The incoming pulse is split with a beam splitter into two beams which travel through the two arms of the Mach-Zehnder interferometer. Each of the arms contains a stage with two mirrors mounted on it. The second arm has been moved away from the rest of a setup introducing thus a time delay between the two pulses. A piezo-driven stage of high accuracy adjusts the distance s of the second arm of the interferometer and the two pulses meet again at a second BS and are guided to the ReMi. Figure is adapted from [Fec14].

been introduced between the two pulses. The relation between the shift in space Δs and the shift in time Δt is:

$$\Delta t = \frac{\Delta s}{c_{air}} \tag{4.12}$$

where $c_{air} = c/n$ is the speed of light in air. The second arm is controlled by a high accuracy piezo-driven stage providing a maximum delay of 3ps with a precision of 80as according to [Cam13]. The two beams are recombined at the second BS and directed to the ReMi. The fact that the second arm of the interferometer is placed quite far away from the rest of the setup and that extra optical elements are required in order to guide the second beam into the BS increases the dispersion. Therefore, a second pair of wedges has to be placed inside the second arm in order to compensate for this effect. Additionally, the intensities of both pulses can be independently controlled by using several irises.

Before performing the experiment, one has to confirm that the two beams spatially and temporally overlap over long distances. For the observation of the interference fringes both arms of the interferometer must have the same length. A setup consisting of several mirrors was buit for the investigation of the spatial and temporal overal of the two beams after they have travelled a distance of a couple of meters.

Two ultrashort ($\sim$ 6fs duration) laser pulses have been created, which propagate with a nanosecond delay with respect to each other. These are guided to the ReMi where they interact with a neutral supersonic gas jet. A description of the ReMi setup and the principles of its operation are the subjects of the following section.

4.2.4 The Reaction Microscope (ReMi)

A very significant part of the experimental setup is the Reaction Microscope (ReMi), which is a highly advanced momentum spectrometer. It allows the simultaneous detection of both ions and electrons emitted by the interaction of the ultrashort laser pulses with the gas jet. The detection over the full 4π solid angle is possible over a large range of kinetic energies. Since ions and electrons originate from the same ionization process they can be detected in coincidence and it is also possible to reconstruct the complete three dimensional momenta of each observed particle with a high resolution. More information about the ReMis can be found in [Dor+02], [MFK03] and [Ull+03] for instance.

4.2.4.1 Setup and some technical specifications

The ReMis used in atomic and molecular physics experiments consist of detectors which are suited for different multiple tasks. For example, investigation of electron and ion collisions is possible or interactions of ultrashort laser pulses with gas jets, radiation originating from high harmonic generation or free-electron lasers interacting with single particles. In all cases, however, the underlying operating principle is the same: projectiles ionize and possibly dissociate target atoms or molecules. The main advantage of this configuration is that the initial momenta of all charged particles can be reconstructed by utilizing the time of flight information and the knowledge of the positions where particles hit the detectors.

A schematic overview of the ReMi used for this experiment is illustrated in figure 4.10. The electric and the magnetic fields are pointing at the z-direction which is referred to as the longitudinal direction and which is also the direction along the laser polarization axis. The direction perpendicular to the spectrometer axis is the transversal direction. The two ultrashort laser pulses created in our experiment are focused onto a dilute supersonic gas jet of argon atoms. The preparation of this gas jet will be presented in a following section. From the interaction of the pulses with the gas jet, ions and electrons emerge which are guided by a homogeneous electric and magnetic field towards two opposing particle detectors. The electric and magnetic field are created by spectrometer anodes and a pair of Helmholtz coils, respectively. The spectrometer has a cylindrical symmetry which is usually the case for various ionization processes.

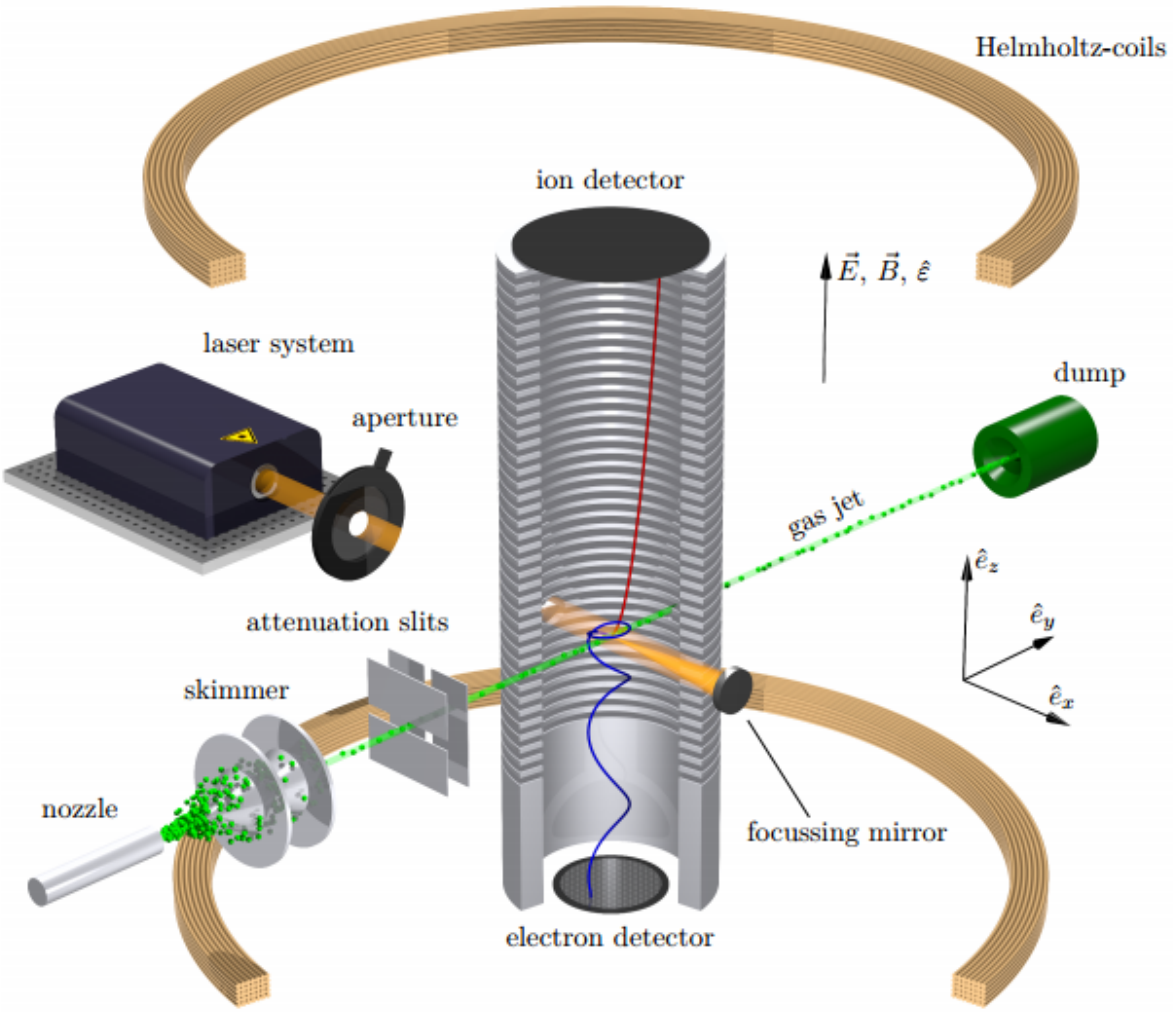

FIGURE 4.10: Schematic overview of the Reaction Microscope (ReMi) setup. A dilute supersonic gas jet emerges from a nozzle and it interacts with the laser light originating from the femtosecond laser system. The products of the reaction, i.e. ions and electrons, are guided to the detectors by a homogeneous electric and a magnetic field. The charged particle detectors consist of microchannel plates and give information about the time of flight and the hit positions of the particles. The figure is taken from [Fec14].

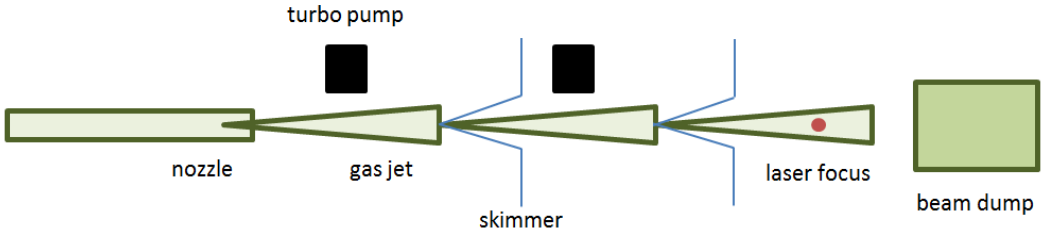

FIGURE 4.11: The supersonic gas jet stage. Supersonic gas expansion takes place after the nozzle. Two skimmers 'shape' the jet and prevent its destruction by shock waves. A beam dump captures all the gas atoms in the jet which are not ionized by the laser maintaining in this way the good vacuum conditions.

The particles are detected by microchannel plate (MCP) detectors. The information we obtain from the MCPs concerns the time of flight of ions and electrons, i.e. the time starting from the moment the reaction takes place until the particle of our interest reaches the detector. Also, the hit position of the charged particles is measured.

The gas jet

The neutral, dilute supersonic gas jet originates from a nozzle and has to travel through a skimmer and an attenuation slit until it crosses with the ultrashort laser pulses delivered from the femtosecond laser system. A schematic overview can be seen in figure 4.11. Initially, the gas jet travels through a nozzle, where it is cooled down by supersonic expansion, to enter the vacuum chamber. The target gas is at room temperature ($\sim$ 300K) with a pressure of around 3bar whilst the diameter of the nozzle is 30μm. The expansion and temperature decrease of the gas jet is quite complex since it depends on various parameters. More details about it can be found in [Mil88]. The next part of the setup is a set of two skimmers. The two conical apertures, with diameters of 200μm and 400μm respectively, form the jet and prevent its destruction by shock waves. They also act as a differential pump stage by seperating the first from the second jet stage. Finally, after the second skimmer the gas jet travels to the main chamber. From there it is dumped in a second chamber, which is separated from the main reaction chamber by a pump, in order to maintain the very low background pressure and preserve the very good vacuum conditions inside the reaction chamber.

The spectrometer

The spectrometer arrangement used in the context of this work is illustrated in figure 4.12. The electric field created by several spectrometer plates accelerates the ions towards the ion detector. A full

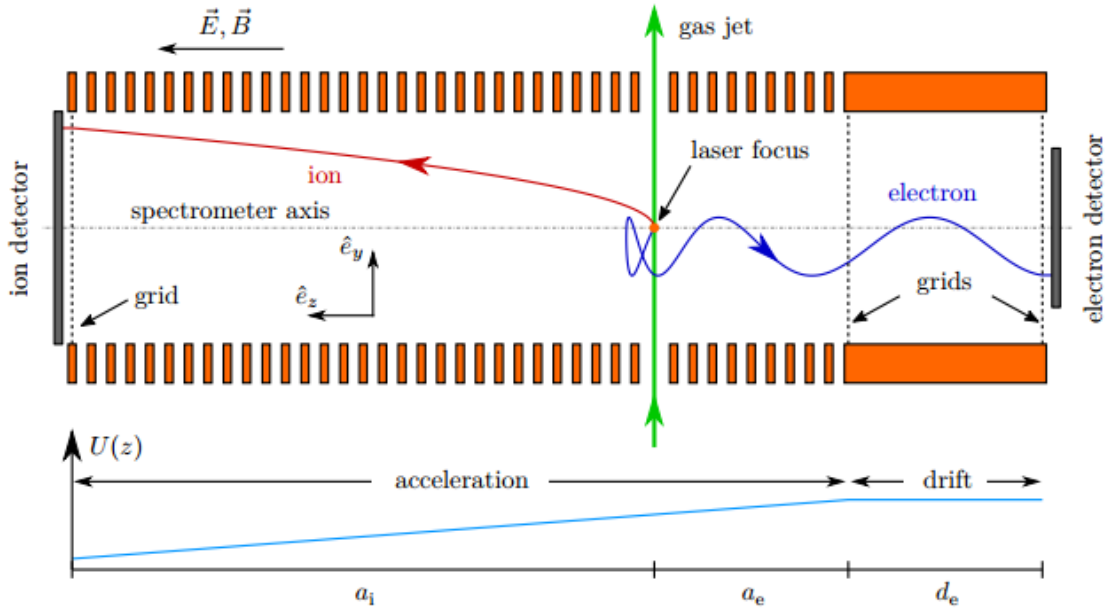

FIGURE 4.12: Schematic overview of the ReMi spectrometer. The electric field is created by several spectrometer plates and guides the ions towards the ion detector (red trajectory). A homogeneous magnetic field causes helical electron trajectories (blue) and guides them to the detector on the right. The dependance of the electric potential U on the coordinate $\hat{e}_z$ along the spectrometer axis can be seen at the lower part of the figure [Fec14].

solid angle acceptance for charged particles is assured. The trajectories of the particles emerging from the reactions at the center of the ReMi are mass-specified. The homogeneity of the electric field inside the spectrometer is ensured by a set of grids which are placed at the two ends of the setup. They suppress field penetrations from the outside and they are placed in such a way, in order to seperate the acceleration from the drift region. Typical photoelectron energies are high in our experiment due to the small mass of the electron and as a result most of the electrons could escape from the spectrometer undetected. However, if the electric field is increased the time of flights of the particles will become shorter and the their spatial distributions smaller. Thus, an additional homogeneous magnetic field created with Helmholtz coils is necessary to maintain a full solid angle acceptance for those particles. The Lorentz force causes cyclotron electron trajectories and guides them to the electron detector.

The ions are accelerated through the whole spectrometer for a distance a_i until they reach the detector. On the other hand, the electrons go through a field-free drift region until they reach the electron detector. If the projectiles gain no extra momentum after the interaction with the laser, then their (TOF) and their hit position information are well defined since their masses and charges are known. Therefore, by combining an electric and a magnetic field the charged fragments are strongly accelerated towards their respective detector.

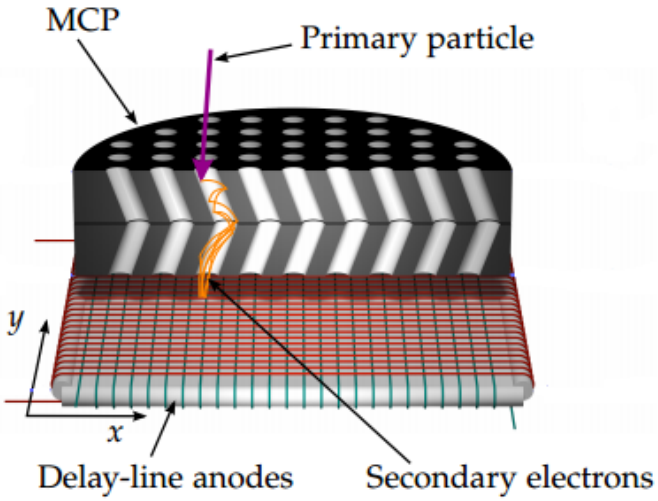

FIGURE 4.13: The MCP detector. It provides information on the TOF and hit position of the charged particles. Initially, a primary particle is impacting on the front side of the MCP. Afterwards an electron cloud is created, i.e. the electrons are multiplied and end up being projected on the delay line anode resulting in a macroscopic current. The figure is adapted from [Cö15].

The micro-channel plate (MCP) detectors

The charged fragments are detected by employing two micro-channel plate (MCP) detectors in chevron (v-like) configuration followed by a pair of delay-line anodes. The MCPs can accurately measure both the impact time and the hit position of each particle. The detection scheme, which can be realized in two steps, is illustrated in figure 4.13. Initially, a charged particle hits the MCP front and an electron cloud is created leading to signal amplification. A high voltage difference between the front and the back surface of the MCP of approximately 1200V causes the channels to act as electron-multipliers. The signal detected at this time gives information on the time of impact, T_{imp} and can be used to determine the TOF of the particle hitting the detector:

$$T_{TOF} = T_{imp} - T_{pulser} + T_0 \tag{4.13}$$

where T_{pulser} is a reference time provided by a photodiode inside the laser system and T_0 is a constant offset. Secondly, the hit position of the charged particle can be determined by measuring the center of gravity of the electron cloud. This can be done by using two perpendicular delay-line anodes which consist of copper wires. The electron cloud impinges on them and one of them is used to measure the x position and the other measures the y position. More information on the two detection steps can be found in [Cam13] and [Fec14].

Chapter 5

Measurement of the isotopic shift of ^{40}Ar and ^{36}Ar

In this chapter the results obtained by measuring the isotopic shift between ^{40}Ar and ^{36}Ar for the $3s^2 3p^5$ $(^2P_{3/2} \rightarrow {}^2P_{1/2})$ transition will be presented. For the realization of this measurement, a Ramsey scheme is introduced creating a coherent superposition of two electronic states, namely a *spin-orbit wave packet* (SOWP) in singly charged argon ions. For the creation of the SOWP a pump-probe experiment is performed where a time-delay is introduced between two ultrashort laser pulses. Detection takes place in the ReMi where the beating is measured with very high accuracy for long delays. The data analysis involves many steps before the calculation of the final result. Those steps will be described in detail in the following sections. In the first part of this chapter, the calibration process required for the analysis will be presented and most of the important parts of the data analysis will be shown. The calibration is initially performed for ^{40}Ar and then applied for ^{36}Ar. ^{36}Ar must be carefully isolated from the TOF spectrum. Each isotope has an oscillatory behavior from which the phase is extracted and plotted versus the data counts. By comparing the two phases we can clearly observe a phase shift. Afterwards, the calculations required for measuring the isotopic shift will be presented. In this experiment, we expect to obtain a 10^6 precision since the laser pulse has a duration of the order of a few fs and the delay that we introduced is of the order of a few ns. Finally, a discussion on the interpretation of the results will be provided at the end of this chapter.

5.1 Data acquisition

The experiment described in the previous chapter is performed. A strong and ultrashort laser pulse of approximately $25fs$ duration and $10^{14}W/cm^2$ intensity is delivered by the femtosecond laser system. It is focused onto a hollow-core glass fiber filled with neon gas at 3 bars of pressure after which the pulse duration is significantly reduced. After the fiber a set of chirped mirrors is utilized to compensate for

dispersion acquired when the pulse propagates through the different optical media.

Then, the pulse propagates through a Mach-Zehnder interferometer. The first pulse (pump) propagates through one arm of the interferometer whilst the second pulse (probe) has to travel through the second arm which has been extended by $119cm$. Therefore, a time-delay is introduced between the two femtosecond pulses that have been created which has a value of $3.97ns$. The two pulses are guided to the ReMi where they interact with a dilute, supersonic argon gas jet which contains the different isotopes at the center of the vacuum chamber. A coherent superposition of the two spin argon states ($^2P_{3/2}$ and $^2P_{1/2}$) is created where the SOWP is beating with a period of approximately 23fs.

The two isotopes of interest are differentiated through mass spectrometry in our spectrometer chamber. The charged particles are guided by an electric field towards two MCPs where detection takes place. In our case, only the ion MCP detector is switched on as electron detection is not necessary for our experiment. The information that can be obtained from the MCP detector is the *time-of-flight* (TOF) of the ions, i.e. the time an ion needs to reach the detector and the x and y position of the ion on the detector.

The experiment is performed several times until optimal conditions are reached in order to measure the isotopic shift as accurately as possible. Optimal conditions include for example optimal alignment of the laser, adjusting the pressure inside the fiber and obtaining the maximum possible power after it. Moreover, compensating for dispersion by placing pairs of wedges at the MZ part of the interferometer and assuring that there is sufficient ionization of argon atoms. All the aforementioned adjustments can increase the number of counts of ionized argon atoms.

Four different data sets are recorded. In the first one, the lengths of the two arms of the MZ interferometer are equal. In the second one, an approximate delay of $30cm$ is introduced between the pump and the probe pulse. For the third and the forth data sets, the second arm of the MZ interferometer has been displaced for approximately $1.2m$. Here, we will present the results acquired from the forth data set for which the longest delay between the two pulses has been introduced. Also, the experimental conditions are better compared to the results obtained from the third data set, i.e. there is sufficient ionization of argon atoms. This is why we choose to show the last data set obtained. Each measurement lasts approximately 16 hours. The data are acquired by a software named *Cobold* and are saved in single files, 21 in total. Each of the 21 files is calibrated since experimental conditions are changing during one measurement as explained before.

The first graph obtained from the ReMi before the data calibration and analysis, is the TOF spectrum of all the ions produced in

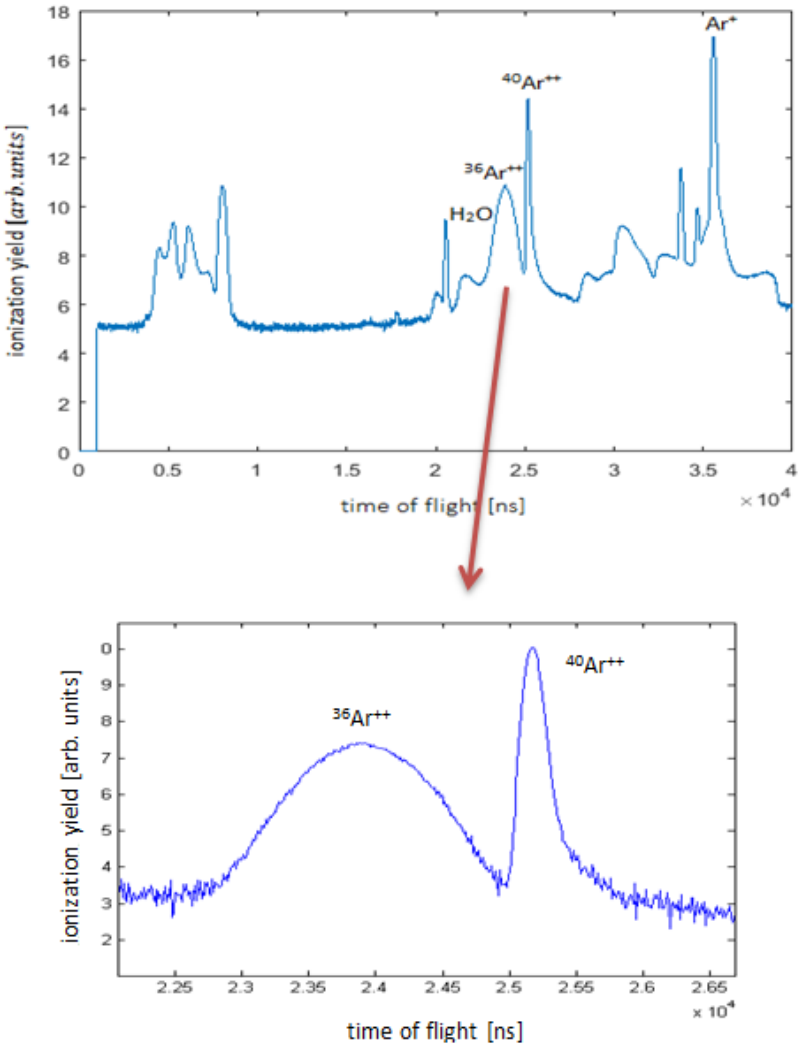

FIGURE 5.1: The *time-of-flight* (TOF) spectrum. The TOF of positively charged ions in ns is plotted versus the ionization yield in logarithmic scale for a laser pulse of approximately $6fs$ duration. All different products of ionization are visible. In the second picture, a zoom in has been performed for the peaks of $^{40}Ar^{++}$ and $^{36}Ar^{++}$, which are the two isotopes of interest for this experiment.

the vacuum chamber. As seen in figure 5.1, the TOF is measured in ns and plotted versus the ionization yield of the ions in logarithmic scale for the first data file. A zoom in has been performed for the two isotopes of interest, namely ^{40}Ar and ^{36}Ar. We observe that the peak of $^{36}Ar^{++}$ and the water peak coincide since they have the same mass-to-charge ratio. However, the H_2O peak is much broader since these molecules have larger initial momenta. Generally, the TOF can be approximated by the equation:

$$TOF \propto \sqrt{\frac{m_i}{q_i}} \tag{5.1}$$

where m_i and q_i represent the mass and the charge of the ion of interest respectively. Therefore, if two charged particles have the same mass-to-charge ratio, their peaks are located in the same TOF region. The fact that the peaks of these two fragments coincide is one of the issues that we had to take into account during the data analysis. The way we dealt with this problem will be described in detail in section 5.2.2, where the calibration process for ^{36}Ar is presented.

5.2 Data calibration

5.2.1 Calibration using ^{40}Ar

Calibration of our data is necessary before being able to analyze them. This is mainly due to the fact that during long measuring times it is possible that the laser gets misaligned, mostly due to temperature fluctuations. When a misaligned laser beam is guided to the MZ interferometer, it is probable that the value of the delay introduced between the two laser pulses changes. Therefore, we have to make sure that we know how this delay changes with time. For this, we use a reference according to which we calibrate our results in order to compensate for such deviations. We create a linear relationship between the phase of the isotope and the MZ positions. For a fixed phase we calibrate the starting position of the MZ. This is set to zero for all 21 files in which the data are saved. Calibration is necessary since it can influence the accuracy of our measurement as well as the statistical error of our result.

Data normalization

For the calibration, we initially worked on the data of ^{40}Ar and then we repeated the exact same procedure for ^{36}Ar with an appropriate adjustment. Working on the first file of the set of 21 files, we initially isolated ^{40}Ar by applying the corresponding TOF condition. We plotted the ionization yield, i.e. the counts as a function of the MZ positions. This can be seen in the first part (red) of figure 5.3

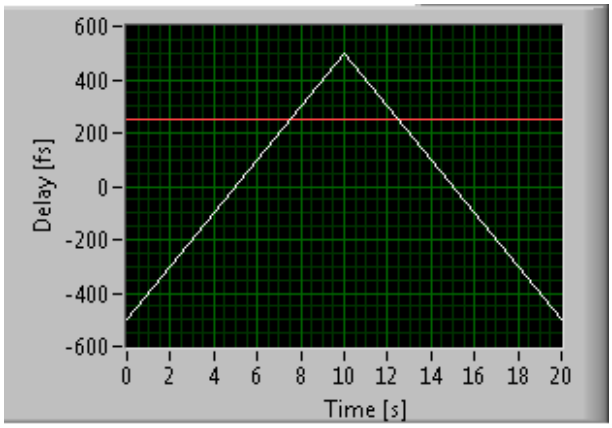

FIGURE 5.2: The position over time of the MZ interferometer can be seen in the figure above. The whitel line of the plot shows the position of the MZ interferometer which scans from bottom to top and vice versa. Here, the scanning range is set from $-500fs$ to $500fs$ and the scanning period to $20s$.

where the oscillation of the SOWP in Ar^{++} is depicted. The number of counts is varying whilst the piezo driven arm of the MZ interferometer scans back and forth with a period of our choice over a few μs. The position over time of the MZ interferometer can be seen in figure 5.2. We can adjust the scan range and the period with which the MZ scans back and forth. The white line of the graph depicts the position of the MZ interferometer. The aforementioned variation in counts occurs because the beginning of a measurement does not coincide with the time at which the MZ starts to scan. So, when we start saving data the MZ is located at a random position of the scanning range. Also, during a measurement which lasts approximately 50 minutes, the MZ interferometer does not go the same number of times over each position and therefore introduces this asymmetry which can be seen in the first plot of figure 5.3 (red). To compensate for this, we had to normalize our data by dividing them by the water background which is present in the chamber as a background gas and can be ionized as well. The water yield can be seen in the second image of the figure 5.3 (blue). It was carefully selected from the TOF conditions so that it does not contain any ions which have oscillatory behavior, like $^{36}Ar^{++}$. Finally, the normalized oscillation for ^{40}Ar is plotted (green). We can observe almost 6.5 oscillations and the period of the SOWP is 23.3fs as already calculated by equation 3.18 in Chapter 3.

Sinusoidal fitting

The next step is to apply a sine fitting function to the normalized results. The aim is to use the coefficients resulting form the fitting in order to fix the value of the phase and calibrate the data according to

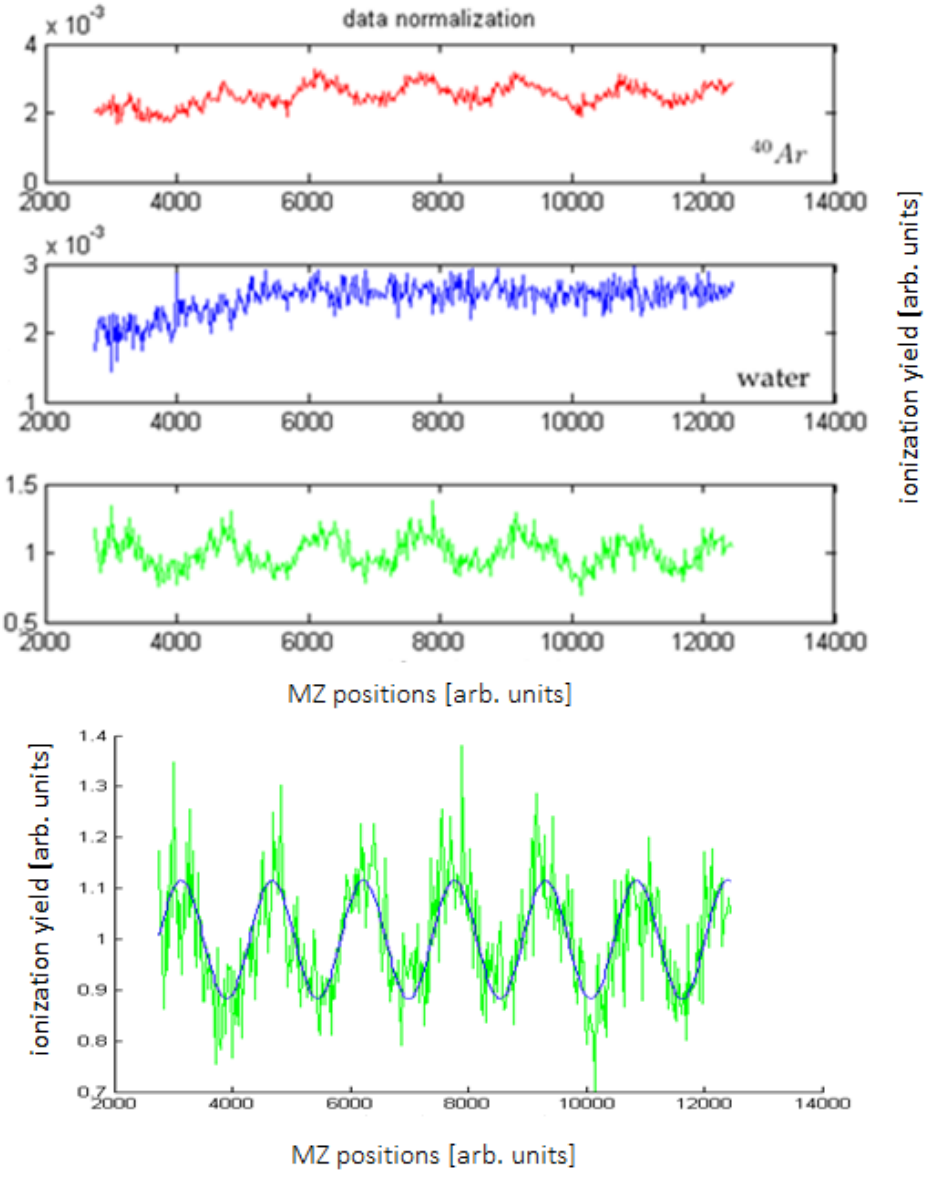

FIGURE 5.3: Data normalization for the case of ^{40}Ar. In the first figure (red) the oscillation of the SOWP in singly charged argon can be seen which has to be normalized. In the second picture (blue) the water present in the chamber as a background gas has been plotted. In the last picture (green), the normalized oscillation of ^{40}Ar can be seen, where the initial data have been divided by the water background. In all cases the MZ positions versus the ionization yield (counts) have been plotted in arbitrary units. In the forth picture a sine fitting has been applied to the normalized data using the nonlinear least-squares formulation.

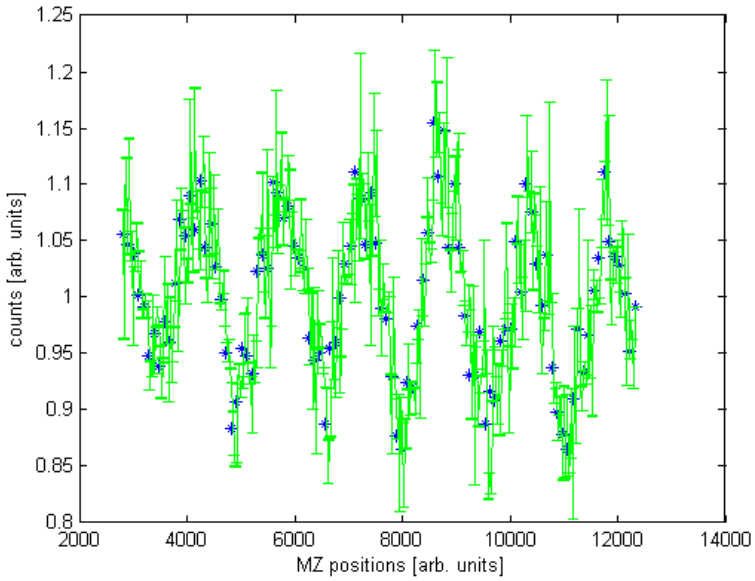

FIGURE 5.4: The SOWP plotted with the corresponding error bars. The data points are the blue points and the error bars are depicted in green.

the starting position of the MZ interferometer. The nonlinear least-squares formulation was used with the typical equation:

$$y = a \cdot sin(2\pi \cdot b \cdot x + c) + d \tag{5.2}$$

where a, b, c, d are the coefficients of the model and x was replaced by the MZ positions. The fitting can be seen in the forth image of figure 5.3. The fitting was repeated for all 21 files. The coeffecients c and d had to be adapted for each set of data, justifying in this way the necessity of the calibration process.

The aforementioned normalization procedure introduces a statistical error which we evaluated. First, we binned our data, i.e. we grouped several values into a smaller number of bins of our choice. The corresponding error bars were inserted, taking into account the propagation of error resulting from the normalization. For the calculation of the propagation of error, here x represents the number of counts corresponding to the first graph of figure 5.3, i.e. the $^{40}Ar^{++}$ yield, y the number of counts corresponding to the second graph of figure 5.3, i.e. the H_2O^+ yield and the quantity$R$ is equal to x/y. The error of each quantity is $\sim \sqrt{x}$ and $\sim \sqrt{y}$ respectively. For the error propagation we used the following formula:

$$\delta R = \mid R \mid \cdot \sqrt{(\frac{\delta x}{x})^2 + (\frac{\delta y}{y})^2} \tag{5.3}$$

The SOWP with the error bars can be seen in figure 5.4. The data are visualized as blue dots and the error bars are depicted in green.

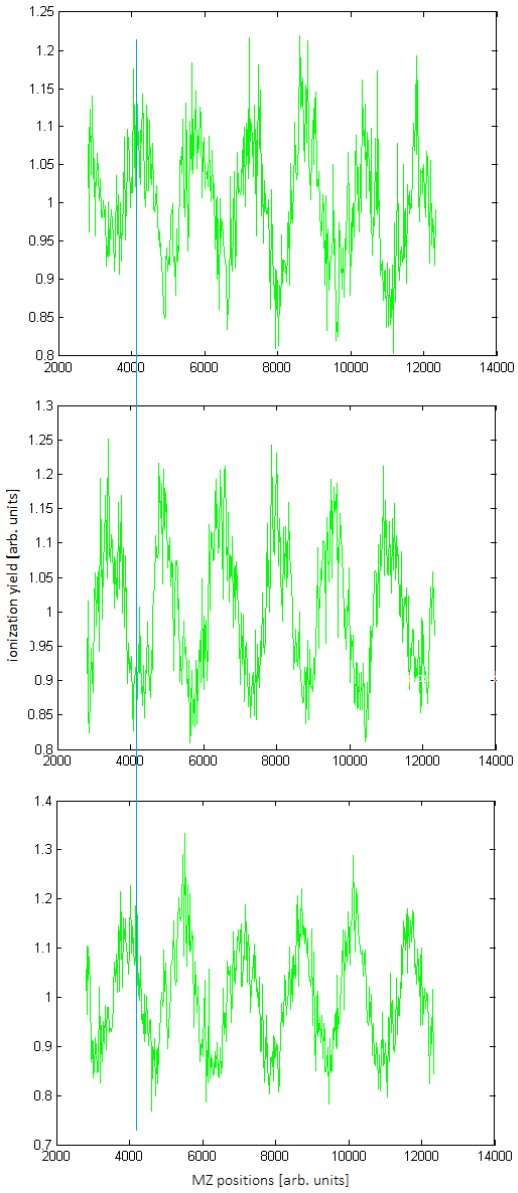

FIGURE 5.5: MZ positions for the first three data files.

Apart from this statistical error, the experiment itelf introduces systematic errors. Finally, it is difficult to estimate how much the total statistical error influences our final result.

Phase calibration

As can be seen in figure 5.5 for each file the MZ positions are different, justifying in this way the need for calibration. The first three data files are depicted for which a shift in the MZ positions can be visualized with the blue line. We expect that there is a shift in the MZ positions within each data file. This could be compensated by dividing our data and repeating the analysis for them. However, in that case, we would have done the calibration with less data counts.

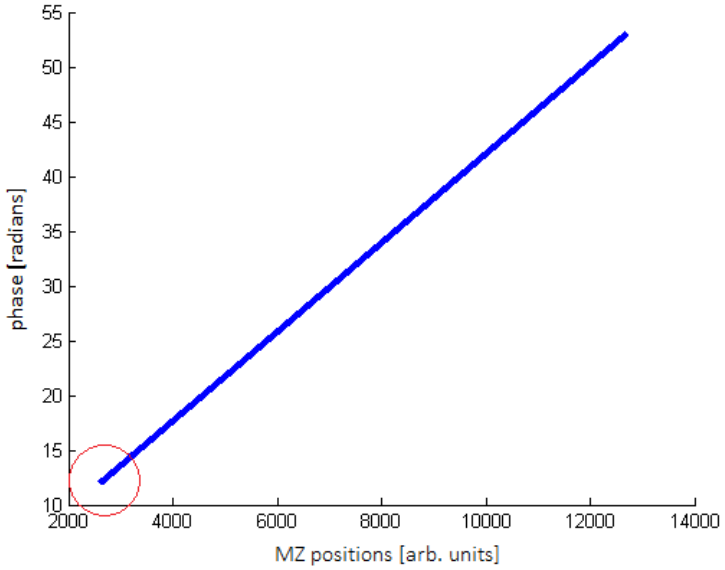

FIGURE 5.6: Data calibration. In this figure the MZ positions are plotted versus the phase. The linear relation that connects them is given by equation 5.4. For each set of files the offset c had to be adjusted so that all graphs coincide according to the first set of files.

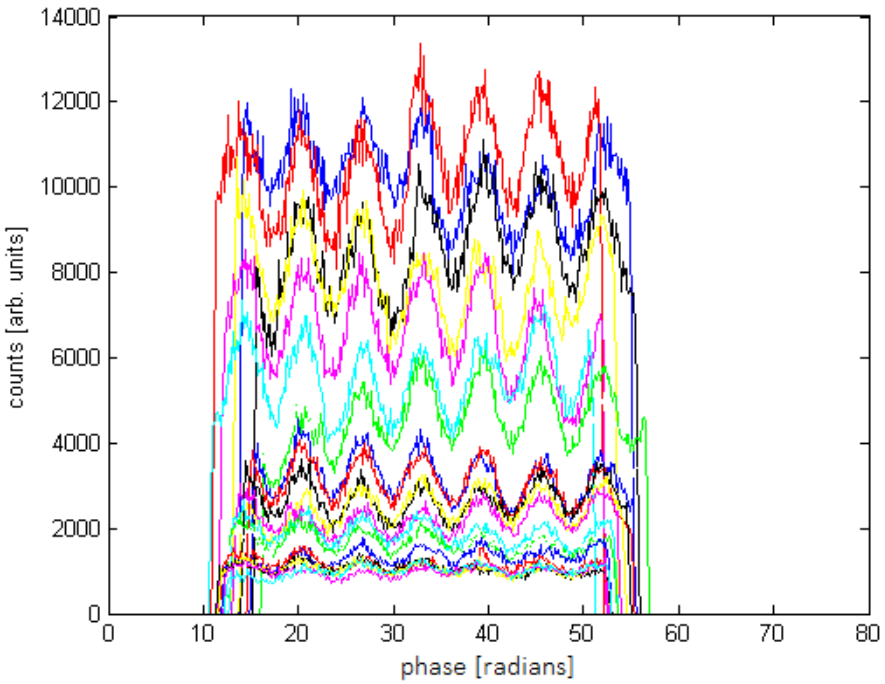

FIGURE 5.7: Plotting the phases of all data sets versus the number of counts.

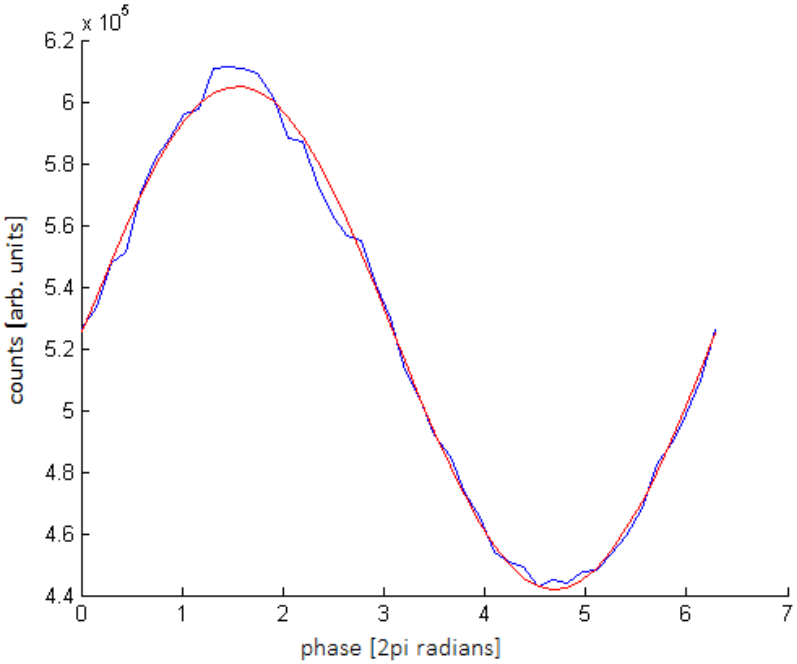

FIGURE 5.8: Phase of ^{40}Ar versus counts. The phase of ^{40}Ar over modulo 2π has been plotted for all calibrated data. From the sine fitting procedure we obtain the value of the coeffecient c which is significant for the analysis.

The MZ positions versus the phase were plotted as seen in figure 5.6. The starting point of the graph is emphasized with a red circle and it is different for all files. At this point the need for calibration becomes more obvious as we have to compensate for this offset and set it to zero for all data sets.

The conversion relation that connects the phase with the MZ positions is given by:

$$phase = MZ_{positions} * b * 2\pi + c \tag{5.4}$$

The coefficients b and c were taken from each one of the sinusoidal fittings performed for all 21 files.

So far, we have created a linear relation between the positions of the piezo-driven arm of the MZ interferometer and the phase. For each set of files we have to adjust the offset c so that all of them coincide with zero. This is the most important step of the calibration. The same procedure was followed for all the 21 files and then they were added up. All the phases were plotted in one graph as seen in figure 5.7.

Phase of ^{40}Ar

Finally, the phase of ^{40}Ar over modulo 2π has been plotted for all our data and a sinusoidal fitting function has been applied to it as

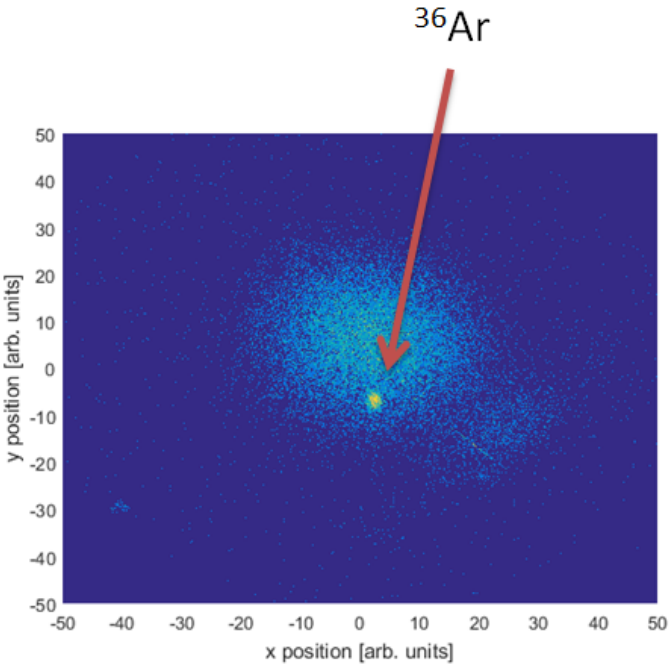

FIGURE 5.9: Position spectrum of ^{36}Ar. The x and y position spectrum of ^{36}Ar has been plotted with the water background. The peaks of the two fragments coincide in the TOF spectrum and it is necessary to seperate them in order to properly calibrate ^{36}Ar.

seen in figure 5.8. The nonlinear least-squares formulation was used again as already described in equation 5.2. The value of the coefficient c arising from the fitting will be necessary for the following analysis as we will see below.

That is the final step for the calibration of the 21 data files using ^{40}Ar. We were interested in creating the same graph for ^{36}Ar in order to compare these two and see whether we can observe any phase shift. Therefore, we had to repeat the procedure of calibration using ^{36}Ar this time.

5.2.2 Calibration using ^{36}Ar

The calibration procedure for ^{36}Ar was exactly the same with the one for ^{40}Ar that was described in the previous section apart from one point. As was already seen in figure 5.1, the peak of ^{36}Ar coincides with the H_2O peak since they have the same mass-to-charge ratio. Therefore, it is necessary to separate the two fragments as precisely as possible. By doing so, we can effectively reduce the background noise and therefore increase the resolution of our data. This separation is achieved by plotting the x, y position image of ^{36}Ar and applying the appropriate x and y conditions so that it is isolated from the H_2O molecule. The x, y position spectrum including the two fragments can be seen in figure 5.9. The corresponding x and y conditions were the same and were applied for all data sets. However, not all

water molecules have been removed since a square shaped area was chosen to isolate ^{36}Ar. This can contribute to the statistical error of the final result and has to be taken into account during the analysis.

After the proper isolation of ^{36}Ar the procedure described in section 5.2.1 is followed once again. Initially, for the first one of the 21 files the ionization yield of ^{36}Ar is plotted and a sinusoidal fitting function is applied to it. The conversion relation between the MZ positions and the phase holds for ^{36}Ar as well. Finally, all the calibrated files are added up and the phase over module 2π is plotted for ^{36}Ar. The comparison between the two graphs for ^{40}Ar and ^{36}Ar and the calculation of the phase shift are the topics of the next section.

5.3 Phase extraction

The two graphs depicting the phase of ^{40}Ar and ^{36}Ar can be seen in figure 5.10. By comparing the phases of the two isotopes a shift is observed. The shift is visualized by the the two black dotted lines. The first one passes through the first maximum of the phase graph of ^{40}Ar and the second one through the first maximum of the phase graph of ^{36}Ar respectively. We compared this measurement with the one obtained for a shorter delay ($\sim 1ns$). We concluded that the shift observed here is the total shift and that there is not a factor of 2π or $n \cdot 2\pi$, with n representing an integer, to add to it.

We also note that the counts of ^{36}Ar are much less compared to ^{40}Ar. This occurs because the abundance of ^{36}Ar is 0.334% whilst the abundance of ^{40}Ar is 99.604% as already mention in Chapter 2.

5.3.1 Measuring the isotopic shift

In order to measure the isotopic shift between ^{40}Ar and ^{36}Ar we first have to obtain the corresponding value of the coefficient c from each graph of figure 5.10. These values arise from the sinusoidal fitting that we have performed for each graph and they are given by:

$$\begin{aligned} c_{40} \pm \delta c_{40} &= 6.30 \pm 0.01 \\ c_{36} \pm \delta c_{36} &= 5.57 \pm 0.06 \end{aligned} \tag{5.5}$$

where the coeffecients are calculated within 95% of the confidence bounds and for their corresponding errors one standard deviation was used to measure the confidence of the statistical error. One standard deviation or 1 sigma means that 68% of the values in the data set lie between the mean value minus 1 sigma and the mean value plus 1 sigma. The phase shift in radians measured from the graph is:

$$shift \pm \delta shift = 0.7330 \pm 0.0608 \tag{5.6}$$

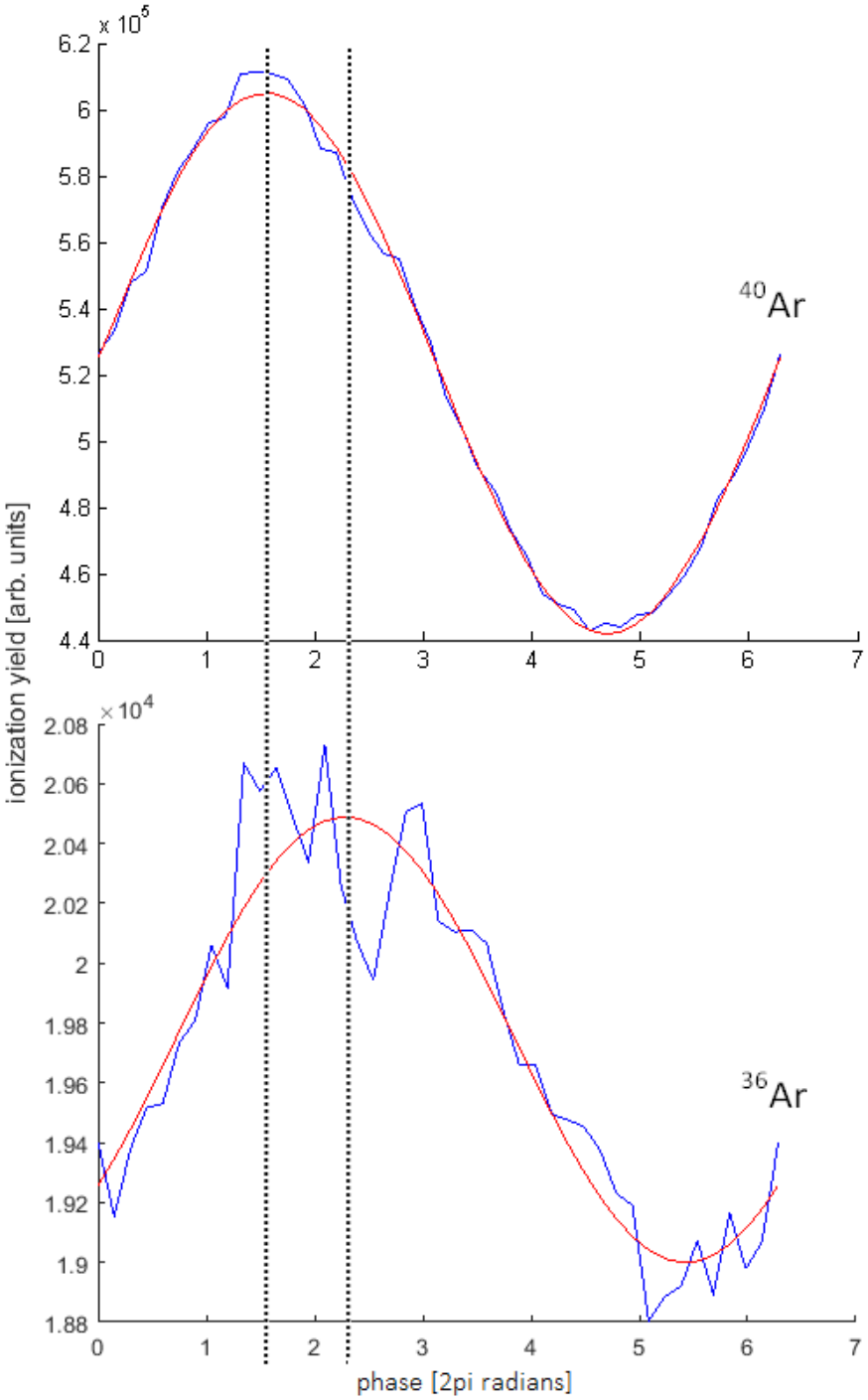

FIGURE 5.10: Isotopic shift between ^{40}Ar and ^{36}Ar. The two black dotted lines indicate the magnitude of the shift. The counts of ^{36}Ar are significantly less compared to those of ^{40}Ar.

The shift is positive since for increasing MZ value the time delay is increasing.

The next step is to 'convert' this shift to time units by taking into account that the oscillation of the SOWP for ^{40}Ar has a period of $T_{40} \pm \delta T_{40} = (23.300365(7) \pm 1.302076(2) \cdot 10^{-5}) fs$ [KRR13]. The measured shift in time is:

$$shift_{time} \pm \delta shift_{time} = \frac{shift \cdot T_{40}}{2\pi} = (2.72 \pm 0.23) \cdot 10^{-15} s \quad (5.7)$$

Additionally, in order to calculate the time delay between the two ultrashort laser pulses we have to estimate how much we have displaced the second arm of the MZ interferometer. This estimation is not very accurate since the time delay has been introduced by manually displacing the mirrors placed on the second stage. A more precise way to determine its value would be by implementing a linear stage. However, as will be shown below in the error analysis this lack of accuracy is not the major contribution to the final error.

The value of the delay is: $length \pm d(length) = (119.0 \pm 2.0) cm$ which corresponds to:

$$delay \pm ddelay = \frac{length}{\frac{c}{n_{air}}} = (3.97 \pm 0.07) ns \quad (5.8)$$

as was already given by equation 4.12. The longer this delay is, the greater the accuracy of our calculation. This occurs since for longer delays, the system has evolved for a longer time, whilst the error remains the same.

The next step is to measure the difference in period between the two isotopes. For the two SOWPs the equations that hold are:

$$\begin{aligned} N_{40} \cdot T_{40} &= delay \\ N_{36} \cdot T_{36} &= delay + shift_{time} \end{aligned} \quad (5.9)$$

where N_{40} and N_{36} are the number of oscillations for ^{40}Ar and ^{36}Ar respectively. The difference in period between the two isotopes is:

$$T_{36} - T_{40} = T_{40} \frac{shift_{time}}{delay} \quad (5.10)$$

We measure the energy difference between the energy of the SOWP of ^{40}Ar and the energy of the SOWP of ^{36}Ar. This energy difference

is the isotopic shift that we calculated between the two isotopes for the $3s^2 3p^5$ $(^2P_{3/2} \rightarrow {}^2P_{1/2})$ transition. Its value is:

$$E_{SO}^{40} - E_{SO}^{36} = IS \pm \delta IS = (1.215102(5) \pm 0.102881(8)) \cdot 10^{-7} eV \quad (5.11)$$

where $E_{SO}^{40} = 2\pi\hbar/T_{40}$ and $E_{SO}^{36} = 2\pi\hbar/T_{36}$ respectively. The period of ^{36}Ar is calculated: $T_{36} \pm \delta T_{36} = (23.300381(7) \pm 1.309061(9) \cdot 10^{-5}) fs$.

The fact that such a small shift was detected by utilizing such a novel technique points out the sensitivity of our method. However, the error calculated is on the order of 10% of our measurement. We were interested in better understanding the different factors that contribute to this error. These are errors originating from the shift itself measured by the sinusoidal fitting, from the delay introduced between the pump and the probe pulse and the errors coming from the oscillation period of ^{40}Ar given in the literature. To estimate the magnitude of each contribution, we set the other two ones to zero. For instance, in order to estimate the contribution from the shift itself, we set the contribution from the delay and the period of ^{40}Ar to zero. Therefore, the shift contributes by a factor of $1.01 \cdot 10^{-8} eV$ to the total error of the IS. Likewise, the contribution of the delay to the error of the IS is $2.04 \cdot 10^{-9} eV$ and the contribution from the period of ^{40}Ar is $6.79 \cdot 10^{-14} eV$.

The biggest contribution arises form measuring the shift itself. The statistics themselves introduce an error to the determination of the coefficient c which has to be taken into account during the calculations that follow. The second biggest contribution to the error of the isotopic shift comes from the delay that we introduced between the two femtosecond laser pulses. It was quite challenging to accurately measure the distance we had moved the second arm of the MZ interferometer due to the complexity of the experimental setup and the amount of optical media between the starting and the ending point of the measurement. Finally, the last contribution originates from the value of T_{40} which is taken from the literature. To calculate it, we used the equation $T_{40} = \frac{2\pi\hbar}{E_{40}}$, where the value of E_{40} for the transition $3s^2 3p^5$ $(^2P_{3/2} \rightarrow {}^2P_{1/2})$ can be found in [Sal10]. Since dE_{40} has been evaluated quite precisely, the contribution of dT_{40} is very small compared to the other contributions to the error.

The isotopic shift in terms of frequency has the value:

$$\Delta f \pm \delta \Delta f = (29.381047(9)) \pm 0.248767(1)) MHz \quad (5.12)$$

Additionally, we calculated the relative shift, i.e. the value of the measurement of the isotopic shift divided by the energy of the

$3s^2 3p^5$ ($^2P_{3/2} \rightarrow {}^2P_{1/2}$) transition for ^{40}Ar. The result is:

$$(\frac{IS}{E^{40}_{SO,NIST}}) \pm (\delta \frac{IS}{E^{40}_{SO,NIST}}) = (0.684589(1) \pm 0.057963(4)) \cdot 10^{-6} \quad (5.13)$$

5.4 Interpreting the results

To the best of our knowledge the measurement of the isotopic shift between ^{40}Ar and ^{36}Ar for the $3s^2 3p^5$ ($^2P_{3/2} \rightarrow {}^2P_{1/2}$) transition using the novel technique that was described in previous chapters has not been mentioned up until now in the existing literature. This is a strong motivation for us since besides calculating this shift we are also interested in understanding its nature and origins. For instance, an accessible quantity that we can calculate and which is already one of the contributions to the IS is the NMS for ^{40}Ar given by equation 2.13. By measuring the relative shift we obtain:

$$(\frac{NMS}{E^{40}_{SO,NIST}}) \pm (\delta \frac{NMS}{E^{40}_{SO,NIST}}) = (1.524652(7) \pm 2.138663(6) \cdot 10^{-7}) \cdot 10^{-6} \quad (5.14)$$

By comparing the last two results (equations 5.13 and 5.14) we observe that the contribution of the NMS is almost twice the total IS which was experimentally measured for the case of ^{40}Ar. Such a discrepancy can be understood when one considers that the total IS consists of the NMS, the SMS and FS contributions as explained in Chapter 2, while here only the contribution of the NMS has been calculated. The SMS term is more complicated to estimate since the correlations between the electron momenta have to be measured for the multielectron atom of Ar, as already explained from equation 2.14. Moreover, we expect that the contribution to the IS from the volume effect is rather small since this effect becomes significant for heavier atoms. However, it should not be neglected in a theoretical calculation as it contributes to the final result. Finally, a complete theoretical analysis should also include the contributions from the relativistic NMS (RNMS) and the relativistic SMS (RSMS).

Finally, the error of the experimental result, which is currently on the order of 10% of the given value, can be significantly improved under certain conditions. A larger delay between the pump and the probe pulse could be introduced ($\sim 10ns$), which could effectively increase the accuracy of the final result. Also, a more accurate and sensitive piezo-driven stage could be implemeted in order to decrease the error in the determination of the delay. And, like all experiments, longer measuring times, i.e. more statistics, could yield in a more precise final result.

Chapter 6

Summary and outlook

The purpose of this thesis was to measure the isotopic shift (IS) between ^{40}Ar and ^{36}Ar for the $3s^2 3p^5$ ($^2P_{3/2} \rightarrow {}^2P_{1/2}$) transition for singly charged argon ions using Ramsey-like spectroscopy. The production and interaction of a strong laser field with argon ions which is created from a Ti:sapphire laser system has been studied whilst the detection takes place in a Reaction Microscope (ReMi).

The femtosecond laser system provided us with strong and short laser pulses ($10^{14} W/cm^2$ intensity, $\sim 6fs$ duration). Inside the laser system, the beam propagates through three different parts (oscillator, amplifier and compressor) which influence its shape and duration. The pulse emerging after travelling through the compressor has a power of $3W$, a repetition rate of $3kHz$ and its duration is increased to $\sim 25fs$.

In order to compensate for the increase in the pulse duration, a neon hollow-core fiber is utilized and placed after the laser system. It enables the production of few-cycle pulses since when the laser pulse has to propagate through it, it interacts with the neon atoms which act as a nonlinear medium. Therefore, they introduce further dispersion into the system as well as other nonlinear effects such as SPM. The spectral width of the beam is broadened allowing in this way the production of shorter pulses. A set of chirped mirrors is placed after the fiber to ensure the compression of the pulses.

Time-resolved measurements are realized with the implementation of a Mach-Zehnder interferometer. At this point the beam travels through a beam-splitter (BS) and is split into two pulses, the pump and the probe, which propagate through the two arms of the setup and meet again at a second BS. In this experiment, one of the arms of the interferometer is displaced by approximately one meter introducing in this way a time delay of $3.97ns$ between the pump and the probe pulse.

The two pulses are then directed to the ReMi where they interacte with a neutral, supersonic and dilute argon gas jet. The pump pulse creates a coherent superposition of the two spin states ($^2P_{3/2}$ and $^2P_{1/2}$), namely a spin-orbit wavepacket (SOWP), which oscillates with a period of $T_{SOWP} = 23.3fs$ for relatively long times without decaying. The second pulse probes the dynamics of the system. Since the oscillation period of the SOWP is of the order of fs and the delay

we introduce is a few ns we expect to acquire an accuracy of 10^6 in our measurement. A mathematical description of the SOWP can be found in the last part of Chapter 3.

The interaction of the femtosecond laser beam with the argon gas jet, including the different isotopes, takes place at the center of the vacuum chamber of the spectrometer and the fragments (argon ions) are guided with an electric field towards the micro-channel-plate (MCP) detector.

In the last Chapter of this thesis the results of this experiment are presented. Before measuring the IS, we had to calibrate our data because during long measuring times the laser could be misaligned which could lead to a shift of the SOWP between the different data sets. After the data analysis the phase modulo over 2π for the two isotopes of interest is plotted, where a phase shift between ^{40}Ar and ^{36}Ar is observed. The phase shift is measured leading to the value of the total IS:

$$E_{SO}^{40} - E_{SO}^{36} = IS \pm dIS = (1.21(510) \pm 0.10(288)) \cdot 10^{-7} eV$$

To the best of our knowledge, this value has not been mentioned anywhere in the literature up until now as far as the ^{40}Ar and ^{36}Ar pair and the $3s^2 3p^5$ ($^2P_{3/2} \rightarrow {}^2P_{1/2}$) transition are concerned. Additionally, we calculated the contribution of the NMS to the total IS, which is approximately a factor of two larger compared to our experimental result.

The contributions to the error of our result are also studied carefully. The main contribrution arises from the shift itself since the fitting method used contains an uncertainty in the determination of the coefficient c which has to be considered during the calculations. The delay we introduce by displacing one of the arms of the MZ interferometer introduces another significant error. One contribution to the error comes from the determination of the period of ^{40}Ar which is however very small compared to the the two aforementioned terms.

Finally, the error of the experimental result, which is currently on the order of 10% of the given value, can be improved under certain conditions. Like all experiments, longer measuring times, i.e. more statistics, could yield in a more precise final result.

Appendix A

A.1 Atomic units (a.u.) and physical constants

In atomic physics expressions can be greatly simplified with the use of atomic units. These can be obtained when the Planck's reduced constant $\hbar$, the electron mass m_e, the elementary charged particle e and the Coulomb's constant k_e are set to unity, i.e.:

$$\hbar = m_e = e = k_e = 1 \tag{A.1}$$

The following table summarizes the most basic quantities and relations used in this work.

quantity	definition	1 a.u. corresponds to
length	Bohr radius a_0	$0.529\,177\,210\,92 \times 10^{-10}$ m
mass	electron mass m_e	$9.109\,382\,91 \times 10^{-31}$ kg
		$1822.888\,48^{-1}$ u
charge	elementary charge e	$1.602\,176\,565 \times 10^{-19}$ C
energy	Hartree energy E_h	$4.359\,744\,3 \times 10^{-18}$ J
		27.211 385 05 eV
angular momentum	$\hbar$	$1.054\,571\,726 \times 10^{-34}$ J s
		$6.582\,119\,28 \times 10^{-16}$ eV s
time	$t = \hbar/E_h$	$2.418\,884\,33 \times 10^{-17}$ s
momentum	$m_e a_0/t$	$1.992\,851\,74 \times 10^{-24}$ kg m/s
electric field	E_h/ea_0	$0.514\,220\,642 \times 10^{12}$ V/m
intensity	$E_h^2/\hbar a_0^2$	$6.436\,409\,1 \times 10^{15}$ W/cm^2
laser intensity*	$\varepsilon_0 c E^2/2$	$3.509\,445\,1 \times 10^{16}$ W/cm^2

*common convention in strong-field physics, see e.g. [Protopapas et al. 1997]

Each physical quantity is defined and connected to another unit system. Picture is taken from [Fec14].

A.2 Particle data

	Ar		Ar^+
E_i [eV]	15.759 611 2	E_i [eV]	27.629 67
mass [u]	39.948	$\Delta\omega$ [eV]	0.177 493 68

Important data for Ar and Ar^+ including masses, the ionization potential E_i and the spin-orbit splitting $\Delta\omega$. Figure adapted from [Fec14].

Bibliography

[ADK86] MV Ammosov, NB Delone, and VP Krainov. "Tunnelling ionization of complex atoms and of atomic ions in an alternating electromagnetic field". In: *Sov. Phys. JETP* 64.6 (1986), pp. 1191–1194.

[Ago+79] Pierre Agostini et al. "Free-free transitions following six-photon ionization of xenon atoms". In: *Physical Review Letters* 42.17 (1979), p. 1127.

[Aro18] Lester Aronberg. "Note on the Spectrum of the Isotopes of Lead". In: *The Astrophysical Journal* 47 (1918), p. 96.

[Bab63] FA Babushkin. "Isotope shift of spectral lines". In: *Sov. Phys.—JETP* 17 (1963), p. 1118.

[BAC50] Ga Breit, GB Arfken, and WW Clendenin. "Spectroscopic isotope shift and nuclear polarization". In: *Physical Review* 78.4 (1950), p. 390.

[Ban06] Yehuda B Band. *Light and Matter: electromagnetism, optics, spectroscopy and lasers*. Vol. 1. John Wiley & Sons, 2006.

[BB76] DR Bates and B Bederson. "ADVANCES IN ATOMIC AND MOLECULAR PHYSICS. VOLUME 12." In: (1976).

[BC76] J Bauche and R-J Champeau. "Recent progress in the theory of atomic isotope shift". In: *Advances in atomic and molecular physics* 12 (1976), pp. 39–86.

[BDF03] JC Berengut, VA Dzuba, and VV Flambaum. "Isotope-shift calculations for atoms with one valence electron". In: *Physical Review A* 68.2 (2003), p. 022502.

[Bj1] URL: https://aqpl.mc2.chalmers.se/~gojo71/KvantInfo/Rabi.pdf.

[BK52] P Brix and H Kopfermann. "Hyperfeinstruktur der Atomterme und Atomlinien". In: *Zahlenwerte und Funktionen aus Physik-Chemie-Astronomie-Geophysik-Technik*. Vol. 1. HH Landolt-Börnstein. Springer Berlin, 1952.

[Bod58] AR Bodmer. "Isotope shift and changes of nuclear radius". In: *Nuclear Physics* 9.3 (1958), pp. 371–390.

[Boy03] Robert W Boyd. *Nonlinear optics*. Academic press, 2003.

[Bre58] Go BreÍt. "Theory of isotope shift". In: *Reviews of Modern Physics* 30.2 (1958), p. 507.

[Bro+74] JH Broadhurst et al. "High resolution measurements of isotope shifts and hyperfine splittings for ytterbium using a cw tunable laser". In: *Journal of Physics B: Atomic and Molecular Physics* 7.18 (1974), p. L513.

[BV66] J BROCHARD and R VETTER. "Use of a variable-length single-cavity laser as an instrument for analyzing isotopic displacements in the infrared(Isotope shifts measurement in IR with variable length laser cavity)". In: (1966).

[Cam13] Nicolas Camus. *Non-sequential double ionization of atoms with phase-controlled ultra-short laser pulses*. PhD Thesis, 2013.

[CK07] PB Corkum and Ferenc Krausz. "Attosecond science". In: *Nature Physics* 3.6 (2007), pp. 381–387.

[Coj03] E Cojocaru. "Analytic expressions for the fourth-and the fifth-order dispersions of crossed prisms pairs". In: *Applied optics* 42.34 (2003), pp. 6910–6914.

[Cor93] Paul B Corkum. "Plasma perspective on strong field multiphoton ionization". In: *Physical Review Letters* 71.13 (1993), p. 1994.

[CS49] MF Crawford and AL Schawlow. "Electron-nuclear potential fields from hyperfine structure". In: *Physical Review* 76.9 (1949), p. 1310.

[Cö15] Philipp Cörlin. *Tracing ultra-fast molecular dynamics in O_2^+ and N_2^+ with XUV–IR pump–probe experiments*. Springer Science & Business Media, 2015.

[Dem13] Wolfgang Demtröder. *Laser spectroscopy: basic concepts and instrumentation*. Springer Science & Business Media, 2013.

[Dor+02] R Dorner et al. "Multiple ionization in strong laser fields". In: *Advances in Atomic Molecular and Optical Physics* 48 (2002), pp. 1–35.

[DPS99] G D'Amico, G Pesce, and A Sasso. "Field shift analysis of visible and near-infrared argon transitions". In: *JOSA B* 16.7 (1999), pp. 1033–1038.

[DR06] Jean-Claude Diels and Wolfgang Rudolph. *Ultrashort laser pulse phenomena*. Academic press, 2006.

[Dra06] Gordon WF Drake. *Springer handbook of atomic, molecular, and optical physics*. Springer Science & Business Media, 2006.

[Fec+14] Lutz Fechner et al. "Strong-field tunneling from a coherent superposition of electronic states". In: *Physical Review Letters* 112.21 (2014), p. 213001.

[Fec14] Lutz Fechner. *High-Resolution Experiments on Strong-Field Ionization of Atoms and Molecules*. Springer Science & Business Media, 2014.

[FHS04] Gerhard Fricke, K Heilig, and Herwig F Schopper. *Nuclear charge radii*. Springer, 2004.

[Fil+16] Livio Filippin et al. "Multiconfiguration calculations of electronic isotope shift factors in Al I". In: *arXiv preprint arXiv:1610.09233* (2016).

[Fle+11] A Fleischer et al. "Probing angular correlations in sequential double ionization". In: *Physical review letters* 107.11 (2011), p. 113003.

[Foo05] Christopher J Foot. *Atomic physics*. Vol. 7. Oxford University Press, 2005.

[Fos51] EW Foster. "Nuclear effects in atomic spectra". In: *Reports on Progress in Physics* 14.1 (1951), p. 288.

[Fra62] EE Fradkin. "ISOTOPIC SHIFT OF SPECTRAL LINES AND THE COMPRESSIBILITY OF DEFORMED NUCLEI". In: *Zhur. Eksptl'. i Teoret. Fiz.* 42 (1962).

[Fre95] PMW French. "The generation of ultrashort laser pulses". In: *Reports on Progress in Physics* 58.2 (1995), p. 169.

[Fri73] B Fricke. "Effect of nuclear motion on the energy eigenvalues in muonic atoms". In: *Physical Review Letters* 30.4 (1973), p. 119.

[Geb+15] Florian Gebert et al. "Precision isotope shift measurements in calcium ions using quantum logic detection schemes". In: *Physical review letters* 115.5 (2015), p. 053003.

[Gha11] Ajoy Ghatak. *Optics*. Science Engineering Math, 2011.

[Gmb] FEMTOLASERS Produktions GmbH. *FEMTOPOWER compact pro CE-PHASE HP/HR Femtosecond Multi-pass Amplifier USER'S MANUAL v. 3.2.* FemtolasersCP.

[Gmb06] FEMTOLASERS Produktions GmbH. *Users's manual for Mirror-dispersion-controlled Ti:Sapphire Oscillator FEMTOSOURCE Rainbow seed.* Femtolasers (2006)., 2006.

[Gri+79] JAR Griffith et al. "Anomalies in the optical isotope shifts of samarium". In: *Journal of Physics B: Atomic and Molecular Physics* 12.1 (1979), p. L1.

[GV75] S Gerstenkorn and J Vergès. "Interprétation des déplacements isotopiques pairs-impairs anormaux dans le spectre d'arc du mercure". In: *Journal de Physique* 36.6 (1975), pp. 481–486.

[HE30] DS Hughes and Carl Eckart. "The effect of the motion of the nucleus on the spectra of Li I and Li II". In: *Physical Review* 36.4 (1930), p. 694.

[HS74] K Heilig and A Steudel. "Changes in mean-square nuclear charge radii from optical isotope shifts". In: *Atomic Data and Nuclear Data Tables* 14.5-6 (1974), pp. 613–638.

[Iva13] Valentin Ivannikov. *Analysis of trapped atom clock with losses*. PhD Thesis, 2013.

[JK38] DA Jackson and H Kuhn. "Hyperfine structure, Zeeman effect and isotope shift in the resonance lines of potassium". In: *Proceedings of the Royal Society of London. Series A, Mathematical and Physical Sciences* (1938), pp. 303–312.

[Joh01] WR Johnson. "Many-Body Calculations of the Isotope Shift". In: (2001).

[KA93] Wolfgang Kaiser and David H Auston. *Ultrashort laser pulses: generation and applications*. Springer, 1993.

[Kel03] Ursula Keller. "Recent developments in compact ultrafast lasers". In: *Nature* 424.6950 (2003), pp. 831–838.

[KEL65] LV KELDYSH. "IONIZATION IN THE FIELD OF A STRONG ELECTROMAGNETIC WAVE". In: *JOURNAL OF EXPERIMENTAL AND THEORETICAL PHYSICS* 20.5 (1965), pp. 1307–1314.

[Kin13] William Holland King. *Isotope shifts in atomic spectra*. Springer Science & Business Media, 2013.

[KK37] Hans Kopfermann and Hubert Krüger. "Über die Anreicherung des Argonisotops Ar36 und den Isotopieverschiebungseffekt im Spektrum des ArI". In: *Zeitschrift für Physik* 105.7-8 (1937), pp. 389–394.

[KRR13] A Kramida, Yu Ralchenko, and J Reader. "NIST atomic spectra database (ver. 5.1)". In: *National Institute of Standards and Technology, Gaithersburg, MD* (2013).

[LK15] Alexandra S Landsman and Ursula Keller. "Attosecond science and the tunnelling time problem". In: *Physics Reports* 547 (2015), pp. 1–24.

[LVF86] SH Lin, AA Villaeys, and Yuichi Fujimura. "Advances in Multi-Photon Processes and Spectroscopy: Volume 16". In: (1986).

[Mai60] Theodore H Maiman. "Stimulated optical radiation in ruby". In: (1960).

[MFK03] Robert Moshammer, Daniel Fischer, and Holger Kollmus. "Recoil-ion momentum spectroscopy and "reaction microscopes"". In: *Many-particle quantum dynamics in atomic and molecular fragmentation*. Springer, 2003, pp. 33–58.

[Mil88] David R Miller. *Free jet sources*. 1988.

[Mou86] Peter F Moulton. "Spectroscopic and laser characteristics of Ti: Al 2 O 3". In: *JOSA B* 3.1 (1986), pp. 125–133.

[Nef+96] Andrei V Nefiodov et al. "Nuclear polarization effects in spectra of multicharged ions". In: *Physics Letters A* 222.4 (1996), pp. 227–232.

[Nis] URL: http://physics.nist.gov/PhysRefData/Handbook/Tables/argontable1.htm.

[Ort+06] R Soria Orts et al. "Exploring relativistic many-body recoil effects in highly charged ions". In: *Physical review letters* 97.10 (2006), p. 103002.

[Pal87] CWP Palmer. "Reformulation of the theory of the mass shift". In: *Journal of Physics B: Atomic and Molecular Physics* 20.22 (1987), p. 5987.

[PS82] CWP Palmer and DN Stacey. "Theory of anomalous isotope shifts in samarium". In: *Journal of Physics B: Atomic and Molecular Physics* 15.7 (1982), p. 997.

[Rab+38] II Rabi et al. "The Magnetic Moments of ${}_3Li^6$, ${}_3Li^7$ and ${}_9F^{19}$". In: *Physical Review* 53.6 (1938), p. 495.

[Rac32] Giulio Racah. "Isotopic displacement and hyperfine structure". In: *Nature (London)* 129 (1932), pp. 723–733.

[Ram50] Norman F Ramsey. "A molecular beam resonance method with separated oscillating fields". In: *Physical Review* 78.6 (1950), p. 695.

[Ram56] NF Ramsey. *Molecular Beams Clarendon*. 1956.

[Ram90] Norman F Ramsey. "Experiments with separated oscillatory fields and hydrogen masers". In: *Reviews of modern physics* 62.3 (1990), p. 541.

[RB32] Jenny E Rosenthal and G Breit. "The isotope shift in hyperfine structure". In: *Physical Review* 41.4 (1932), p. 459.

[Rie06] Fritz Riehle. *Frequency standards: basics and applications*. John Wiley & Sons, 2006.

[RL14] Theodore W Richards and Max E Lembert. "THE ATOMIC WEIGHT OF LEAD OF RADIOACTIVE ORIGIN." In: *Journal of the American Chemical Society* 36.7 (1914), pp. 1329–1344.

[RS09] Nina Rohringer and Robin Santra. "Multichannel coherence in strong-field ionization". In: *Physical Review A* 79.5 (2009), p. 053402.

[Rul+05] Claude Rulliere et al. *Femtosecond laser pulses*. Springer, 2005.

[Sal10] EB Saloman. "Energy Levels and Observed Spectral Lines of Ionized Argon, ArII through ArXVIII". In: *Journal of Physical and Chemical Reference Data* 39.3 (2010), p. 033101.

[SH76] Orazio Svelto and David C Hanna. *Principles of lasers*. Springer, 1976.

[Sha98] VM Shabaev. "QED theory of the nuclear recoil effect in atoms". In: *Physical Review A* 57.1 (1998), p. 59.

[Shc09] Ihar Shchatsinin. "Free clusters and free molecules in strong, shaped laser fields". PhD thesis. Freie Universität Berlin, 2009.

[She+82] EB Shera et al. "Charge distributions of barium isotopes from muonic X-rays". In: *Physics Letters B* 112.2 (1982), pp. 124–128.

[SKS91] David E Spence, P Np Kean, and Wilson Sibbett. "60-fsec pulse generation from a self-mode-locked Ti: sapphire laser". In: *Optics letters* 16.1 (1991), pp. 42–44.

[SM85] Donna Strickland and Gerard Mourou. "Compression of amplified chirped optical pulses". In: *Optics communications* 56.3 (1985), pp. 219–221.

[Sod13] Frederick Soddy. "Intra-atomic charge". In: *Nature* 92.2301 (1913), pp. 399–400.

[SS73] JD Silver and DN Stacey. "Isotope shift and hyperfine structure in the atomic spectrum of tin". In: *Proceedings of the Royal Society of London A: Mathematical, Physical and Engineering Sciences*. Vol. 332. 1588. The Royal Society. 1973, pp. 129–138.

[Tup+03] II Tupitsyn et al. "Relativistic calculations of isotope shifts in highly charged ions". In: *Physical Review A* 68.2 (2003), p. 022511.

[TZL02] Xiao-Min Tong, ZX Zhao, and Chii-Dong Lin. "Theory of molecular tunneling ionization". In: *Physical Review A* 66.3 (2002), p. 033402.

[Ull+03] Joachim Ullrich et al. "Recoil-ion and electron momentum spectroscopy: reaction-microscopes". In: *Reports on Progress in Physics* 66.9 (2003), p. 1463.

[VHU99] I Velchev, W Hogervorst, and W Ubachs. "Precision VUV spectroscopy of Ar I at 105 nm". In: *Journal of Physics B: Atomic, Molecular and Optical Physics* 32.17 (1999), p. L511.

[Vil+93] Petrine Villemoes et al. "Isotope shifts and hyperfine structure of 134-138Ba II by fast ion beam-laser spectroscopy". In: *Journal of Physics B: Atomic, Molecular and Optical Physics* 26.22 (1993), p. 4289.

[Wal+94] Barry Walker et al. "Precision measurement of strong field double ionization of helium". In: *Physical review letters* 73.9 (1994), p. 1227.

[Wan+14] Yong Wan et al. "Precision spectroscopy by photon-recoil signal amplification". In: *Nature communications* 5 (2014).

[WC11] HJ Wörner and PB Corkum. "Imaging and controlling multielectron dynamics by laser-induced tunnel ionization". In: *Journal of Physics B: Atomic, Molecular and Optical Physics* 44.4 (2011), p. 041001.

[Wen+06] H Wen et al. "Observing angular precession of a Rydberg wave packet due to spin-orbit coupling by orthogonally polarized weak half-cycle pulses". In: *Physical Review A* 73.5 (2006), p. 052504.

[Wil68] M Wilson. "Ab initio calculation of screening effects on— ψ (0)— 2 for heavy atoms". In: *Physical Review* 176.1 (1968), p. 58.

[Zeh91] Ludwig Zehnder. *Ein neuer interferenzrefraktor*. Springer, 1891.

Acknowledgements

First of all, I would like to express my sincere gratitude to the head of the Quantum Dynamics and Control group at the Max-Planck-Institute für Kernphysik, Thomas Pfeifer. He gave me the opportunity to be part of his group and was very supportive and enthusiastic throughout the course of my master thesis. He has created an amazing working environment and he constantly motivates and inspires his students and colleagues.

Mostly, I would like to thank my direct supervisor Robert Moshammer for introducing me to the topic of my master thesis and for his useful comments and engagement through the learning process of the project. The door of his office was always open whenever I ran into trouble or had any question concerning the experiment or writing. His remarks were always to the point, helping me understand the fundamental physics behind every process.

I would also like to thank José Ramón Crespo López-Urrutia for his comments, advice and insight concerning the isotopic shifts. He always helped me with enthusiasm and the fruitful discussions with him were of great assistance for our project. I am also grateful to him for accepting to be the second referee of this thesis.

Most of all, I would like to thank my daily supervisor, Nicola Camus, for his exemplary guidance, monitoring and constant encouragement during my master thesis. His ideas and suggestions helped me fulfill this project and improve my skills concerning experimental physics, programming and scientific writing. He was very patient with my questions and always gave time to assist me in the experiment or review my work. Merci beaucoup!

My sincere thanks also goes to Lutz Fechner who introduced me into his project and assisted me with Matlab. Yonghao who initially helped me with the laser. My office colleague Patrick who was always kind and helpful, Marvin who reviewed my thesis, Ana Denhi and Frans for his assistance with German. Also, Bernd Knap for his technical support.

I would like to thank my loved ones, Eleni, Aliki and Dimitris who have supported me throughout the entire process, both by keeping me harmonious and helping me putting pieces together.

Finally, I must express my very profound gratitude to Maristella, Elpida and Yiannis for providing me with unfailing support and continuous encouragement throughout my years of study and through the process of researching and writing this thesis. This accomplishment would not have been possible without them.

$\Sigma\alpha\varsigma\ \epsilon\upsilon\chi\alpha\rho\iota\sigma\tau\omega\ \pi o\lambda\upsilon$!

Erklärung:

Ich versichere, dass ich diese Arbeit selbstständig verfasst habe und keine anderen als die angegebenen Quellen und Hilfsmittel benutzt habe.

Heidelberg, den (Datum) .....